Leopold-Franzens-Universität

universität
innsbruck

Masterarbeit
zur Erlangung des akademischen Grades
Master of Science
(MSc)
eingereicht an der Fakultät für Mathematik, Informatik
und Physik der Universität Innsbruck

Dipole-Coupled Nano-Ring(s) of Quantum Emitters

von
Cremer, Julian

October 15, 2019

Betreuer:
Univ. Prof. Dr. Helmut Ritsch
Mitwirkende Betreuer:
David Plankensteiner, PhD.
Laurin Ostermann, PhD.
Institut für Theoretische Physik

Abstract

In this master thesis we study the radiative properties of an ensemble of quantum emitters. In particular we are interested in the super- as well as the subradiant collective modes of rings of dipole-coupled subwavelength-spaced atoms.
First we investigate the behavior of the collective decay rates depending on the distance as well as the dipole orientations of the atoms to each other. The collective decay rate increases for superradiant modes for smaller inter-atomic distances and decreases for subradiant modes, respectively. For transverse dipole polarization we can find one very bright mode, whereas tangential dipole polarization show two bright modes. By adding more atoms, the system becomes linearly more superradiant for the explicit modes. Then we look up the state population of the modes for a free evolving system, first without and finally for a disordered geometry. We notice, that for certain parameters the decay rate in a disordered system gets further suppressed. In a next step, we drive the system coherently with a laser and develope a state preparation scheme, in which we can address the subradiant state nearly perfectly. So far, we restricted ourselves to the single-excitation subspace. Therefore we expand our model to study the two-excitations manifold in the same fashion as before. The subradiant properties of the system show a significant downgrade. Finally, we study the radiation field patterns of the collective modes, which exhibit a 3D confined spatial radiation field forming a nano-scale high Q optical resonator.
We then focus on the excitation dynamics of two coupled rings. We can find a variable complex coupling pattern by tailoring the geometry, orientation and distance between the two rings. Superradiant and subradiant modes mostly couple effectively to its own kind with opposite angular momentum. Using this, we also show that completely delocalized subradiant excitations are effectively transported between the rings with high fidelity. We also show the remarkable radiation patterns for two coupled rings.
Finally, we expand our model to a multi-ring configuration and recreate a structure like the so called Light-Harvesting-Complexes (LHCs) in a very simplistic way. Here we have eight outer rings commonly coupled to an inner ring. Here we once more analyze the radiation patterns.
The methods used in this thesis are mainly numerical. For this we applied the Julia programming language and the built-in framework QuantumOptics, developed in the group of Helmut Ritsch [1].

Zusammenfassung

In der vorliegenden Masterarbeit untersuchen wir die superradianten und insbesondere subradianten kollektiven Moden eines Ringes aus dipolgekoppelten zwei-level Atomen im Subwellenlängen-Regime.

Zunächst untersuchen wir das Verhalten der kollektiven Zerfallsraten in Abhängigkeit von dem Abstand, sowie der Dipolorientierungen der Atome zueinander. Die kollektive Abklingrate erhöht sich für Superradiant-Moden durch Verringern des Atomabstandes bzw. verringert sich für Subradiant-Moden. Für transversale Dipolpolarisationen können wir eine helle Mode finden, während tangentiale Dipolpolarisationen zwei helle Moden zeigen. Durch Hinzufügen von mehr Atomen wird das System für die expliziten Modi linear mehr superradiant. Des Weiteren untersuchen wir das Strahlungsfeldmuster der kollektiven Moden, die ein räumlich begrenztes 3D-Strahlungsfeld aufweisen, das einen nanoskaligen optischen Resonator im high Q Regime bildet. In einem nächsten Schritt analysieren wir das Verhalten des Systems, wenn wir eine Dephasierung in den Hamilton-Ausdruck aufnehmen. Bisher haben wir uns auf den Einzelanregungs-Subraum beschränkt. Daher untersuchen wir im letzten Teil dieses Abschnittes unser System in der Mehrfachanregungs-Mannigfaltigkeit. Hier finden wir keine unerwarteten Eigenschaften divergent zum Einzelanregungsfall. Die subradianten Eigenschaften des System verschelchtern sich.

Wir konzentrieren uns im nächsten Abschnitt auf die Untersuchung des Verhaltens von zwei gekoppelten Ringen, wobei wir ein signifikantes Kopplungsmuster finden, indem wir die Geometrie, Orientierung und den Abstand zwischen den beiden Ringen anpassen. Superradiant- und Subradiant-Modi koppeln meist effektiv mit entgegengesetztem Drehimpuls zu ihrer eigenen Art. Auf diese Weise zeigen wir auch, dass vollständig delokalisierte subradiante Anregungen mit hoher Fidelity effektiv zwischen den Ringen transportiert werden.

Schließlich erweitern wir unser Modell und versuchen den sogenannten Light-Harvesting-Complex (LHC) in deutlich simplifizierter Form nachzubilden, bei der acht äußere Ringe gemeinsam mit einem inneren Ring verbunden sind. Hier analysieren wir wiederum das Strahlungsmuster.

Danksagungen

Zunächst möchte ich an dieser Stelle meinen Eltern herzlich danken, ohne die meine Studien nicht möglich gewesen wäre.

Außerdem sei allen Mitgliedern der Arbeitsgruppe gedankt, die mich sehr freundlich aufgenommen haben, immer für Fragen offen und sehr hilfsbereit waren. Insbesondere möchte ich David Plankensteiner sowie Laurin Ostermann danken, die mir stets mit Rat und Tat und vor allem ihrer Programmiererfahrung zur Seite standen.

Danken möchte ich zudem Prof. Helmut Ritsch für die Aufnahme in diese tolle Arbeitsgruppe und für die Idee und Leitgedanken zu dieser Masterarbeit.

Abschließend möchte ich mich bei allen meinen Freunden bedanken, mit denen ich meine Freizeit außerhalb der Physik teilen durfte.

Danke Euch allen.

Contents

1 Introduction **1**

2 Theoretical concepts **4**
2.1 Collective atom-electric Field Coupling 4
2.2 Dipole-dipole Interaction 8
2.3 Master Equation 9
2.4 The System 10
2.4.1 Single Ring 10
2.4.2 Two coupled Rings 12

3 Single Ring: Collective Excitations and radiative Properties **14**
3.1 Collective Dynamics - Single-Excitation Manifold 14
3.1.1 Geometrical Properties 14
3.1.2 Decay from a superradiant as well as subradiant State 18
3.1.3 State preparation 23
3.2 Collective Dynamics - Two-Excitations Manifold 29
3.2.1 Some Characteristics of the Eigenvalues in the Two-excitations Manifold 29
3.3 Radiative Properties 31

4 Two Coupled Rings - Coupling Behavior, Excitation Transfer and Radiative Properties **35**
4.1 Coupling Behavior 35
4.2 Excitation Transfer 39
4.3 Radiative Properties 42

5 Conclusion **43**

6 Appendices **45**
6.1 Appendix A - Program Examples 45
6.2 Appendix B - Multi-ring: A simplistic Recreation of LHCs 51

1 Introduction

One of the central goals in the field of quantum optics is to find efficient ways for controllable interactions between photons and atoms. Since a single quantum emitter in general possesses a non-vanishing dipole coupling to the electromagnetic field and modifies that field in turn, all nearby quantum emitters can feel each other in that sense. Thus by congregating multiple emitters spatially close to one another, the individual behavior changes dramatically culminating in collective correlated dynamics. This is an important factor, that has to be considered when treating an ensemble of quantum emitters.

The most challenging part in controlling interactions between photons and an ensemble of emitters lies in the ability of atoms to radiate spontaneously. In an intuitive picture this decay can be considered as caused by vacuum fluctuations of the electromagnetic field. So, even if the field is in the vacuum mode, spontaneous emission still occurs. In many applications this is not a desirable process, since one has not any control over it. For some time, in quantum optics, one described those rescattering events as if they were occuring independently with a rate given by a single isolated atom. But this assumption concurrently determines the limits of the fidelity of photon-atom-interactions, like it would be important in quantum memories for light or photonic quantum gates for quantum computing [2].

However, it turns out, that this assumption is not tenable at all, since collective interference phenomena have to be taken into account. In fact, shown in the work of Dicke [3], an enhanced radiative behavior was already proposed decades ago, the so called ”superradiance”. Here, constructive interference of fields emitted by different atoms leads to a significant decrease in the lifetime of the collective mode. On the other hand, spontaneous emission of collective atomic excitations can also be completely suppressed, a phenomenon called ”subradiance”, where destructive interference prevents the collective mode from decaying. Although this concept of subradiance is not a new discovery, it has not well researched so far. Therefore, for a good understanding of how to achieve efficient, controlled photon-atom-interactions, it is crucial to study and understand the super- and especially subradiant properties of the systems of concern. And since single photons and atoms do not interact efficiently, it is rather helpful to use larger atomic ensembles, where the interaction probability with a given optical mode can be enhanced by increasing the number of atoms [4].

Dealing with atomic ensembles and their properties for developing error-restraining protocols is a truly severe venture, in particular for the case of trying to take advantage of the subradiant properties, since manipulating each atom seperatly in the ensemble of emitters in order to address collective states of low symmetry is quite a challenge especially experimentally. Nevertheless, there is a step-by-step progress noticeable in recent experiments anyway [5] [6] [7]. Besides that, some demonstrations of succesful quantum protocols have been performed as well, like coherent photon storage and quantum memories for light [4] [8] [9], entanglement generation between light and atomic spins [10], nonlinear interactions between photons at the level of individual quanta [11], and quantum-enhanced metrology [12].

For many applications like quantum communication as well as photosynthetic processes it is highly relevant to minimize the energy loss by providing an efficient way to transfer the systems' energy. In the Förster mechanism for example, a virtual photon is exchanged between closely lying donors and acceptors, whereby the resonant energy transfer efficiency is inversely proportional to the sixth power of the distance among them. So, the energy loss can be optimized by placing them close enough [13]. Further it has been proven, that a system of two distant single layer arrays of subwavelength-spaced quantum emitters supports a long-lived Bell state, which can be seen as a non-local excitation of the two arrays [14]. This resource of non-local entangelement provides a quantum state transfer with high fidelity between the arrays, which can be used as a Quantum memory for Quantum networking for example [14]. For subwavelength-spaced quantum emitters in a infinite 1D-chain, excitations are transferred without any loss, since the guided modes are decoupled from the optical modes propagating in free-space and the excitons become perfectly dark, when their wave vector surpasses the free-space photon wave vector [2]. Contrary to the case of the infinite chain, the lifetime of an exciton in a finite 1D-chain of subwavelength-spaced quantum emitters is growing with the third power of the atom number and emission occurs only at its ends [2]. This has been studied experimentally for chains of gold nano-particles [15].

Now the question arises, what happens, if we close the chain forming a ring of quantum emitters. Answering that is the task of this underlying work. Therefore we utilize the dipole-dipole coupling of nearby identical emitters in a regular-spaced ring configuration and study the emergence of the already mentioned phenomena of super- and subradiance as well as the broadening of the collecive energy spectrum. As a central goal, we analyse the excitation transfer between two separated rings. A ring of subwavelength-spaced dipole-coupled quantum emitters implements a minimalistic form of an optical ring resonator, which in principle can exchange energy with a second nearby ring. We want to examine in which way the rings can be efficiently coupled via their mode overlap by keeping the free-space radiation loss at its minimum. For distributed quantum computing for example a efficient coherent coupling between two long-lived states is a key element and of particular interest [16].

Interestingly, photsynthetic units built by light-harvesting complexes like LHC-I and LHC-II in biological systems, depicted in Figure 1.1a, show, in a very simplistic model, a structure of a large inner ring, that is surrounded by for example eigth outer rings, depicted in Figure 1.1b [17] [18] [19]. The coherent transfer of excitations in such systems could already be shown [19].

In summary, in this underlying thesis, we study the collective behavior of an ensemble of dipole-coupled quantum emitters arranged in a ring configuration. The upcoming first chapter contains the theoretical concepts that are needed for this master thesis as well as the description of the model we are using.

The next chapter provides an examination of the single ring, where we discuss the collective decay rates as a function of diverse geometrical arrangements as well as the radiation fields in the single-excitation manifold. We investigate the system also when it is driven with a coherent laser and show a way of highly efficient state preparation.

Later we extend the model by implementing more than one possible excitation and show some properties of the system in the many-excitations manifold.

In chapter 4 we study the system of two coupled rings. Here we examine the coupling

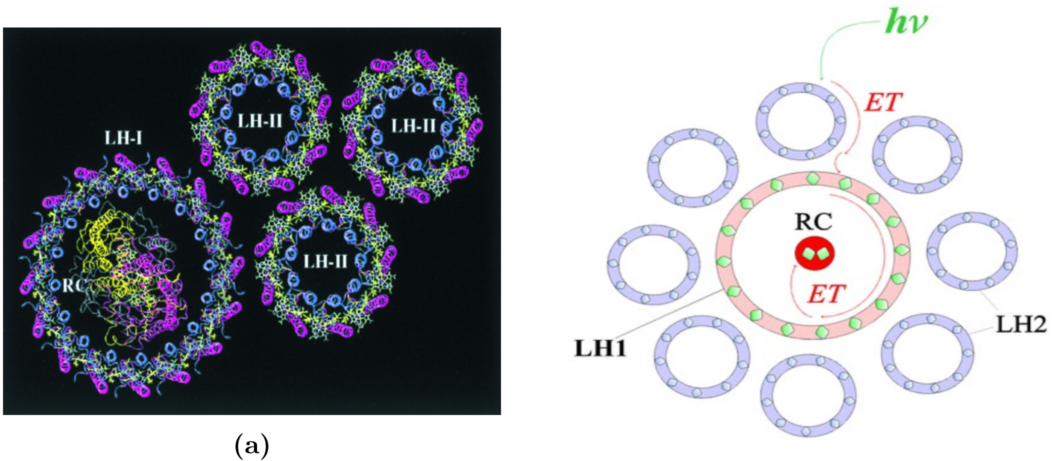

(a)

(b)

Figure 1.1: *Light harvesting complexes in biological systems.* - Arrangement of LH1 and LH2 units in the photosynthetic complex. LH2 units consisting of 9 sites and LH1 units consisting of 16 sites. RC is the so-called reaction centre [18].

behavior and finally show a coherent excitation transfer between the rings as well as the radiation patterns.

2 Theoretical concepts

The main goal of this chapter is to provide a overview of the fundamental theoretical concepts, that are applied in the subsequent studies. Since we are dealing with subwavelength-spaced dipole-coupled two-level quantum emitters, we concentrate here on the description of an ensemble of emitters that is spatially dense, so each emitter experiences the field radiated by all others. In order to do so, we derive the electric field radiated by the entirety of the emitters, where interference phenomena are included.

2.1 Collective atom-electric Field Coupling

Collective interactions of quantum emitters are basically interactions with a common radiation field, where an emitter couples with its dipole transition operator to the electric field modes. Therefore the Hamiltonian can be written as

$$H = H_0 + H_{\text{int}} + H_{\text{em}}, \tag{2.1}$$

where for the reduced Hilbert space considering only the two basis states $|g\rangle$ and $|e\rangle$ with eigenvalues E_g and E_e, respectively, we can write

$$H_0 := E_e |e\rangle \langle e| + E_g |g\rangle \langle g| , \tag{2.2}$$

which describes the kinetic as well as the potential energy of the emitter and

$$H_{\text{int}} = \vec{d} \cdot \vec{E}(\vec{0}, t) = \vec{\mu}(\sigma^\dagger + \sigma) \cdot \vec{E}(\vec{0}, t) \tag{2.3}$$

describes the interaction between the electric field and the dipole transition with dipole moment, which we consider to be real, $\vec{d} := \vec{d_{eg}} |e\rangle \langle g| + \vec{d_{eg}}^{\,*} |g\rangle \langle e|$, where $\vec{\mu} = \vec{d_{eg}}$ is the non-zero dipole transition matrix element and $\sigma := |g\rangle \langle e|$ corresponds to the transition from the excited to the ground state. For the free electric field, which can be separated into forward and backward propagating terms, we have

$$\vec{E}(\vec{r}, t) = \vec{E^+}(\vec{r}, t) + \vec{E^-}(\vec{r}, t), \tag{2.4}$$

where for a arbitrary region in space of volume V $= L^3$, shown in Figure 2.1a, the E^+-term can be written in a mode expansion as

$$\vec{E}^+(\vec{r}, t) = \sum_{\vec{k},\lambda} \sqrt{\frac{\hbar\omega_k}{2\epsilon_0 V}} \vec{e}_{\vec{k},\lambda} e^{i\vec{k}\cdot\vec{r}} a_{\vec{k},\lambda}(t), \tag{2.5}$$

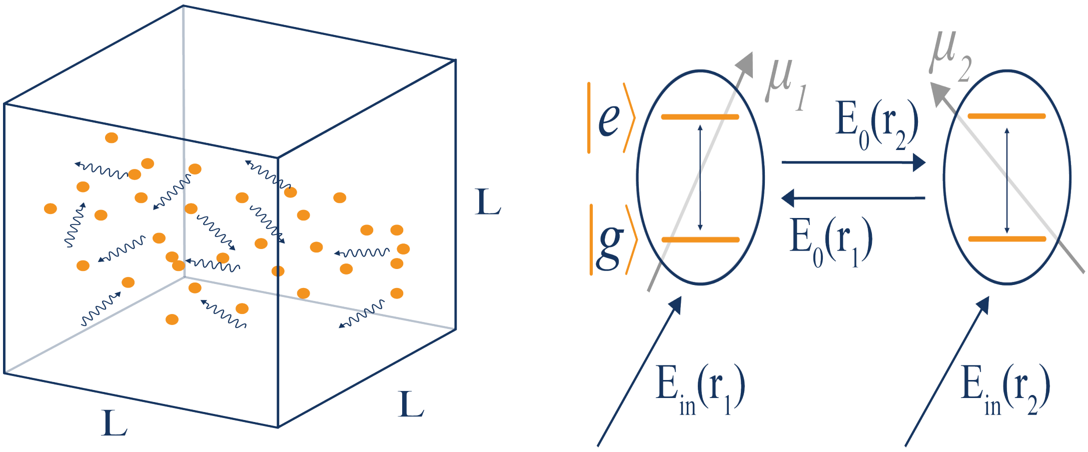

(a) **(b)**

Figure 2.1: Two-level quantum emitters. - (a) Ensemble of nearby quantum emitters in a volume V = L^3 experiencing the collective interference fields of one another. (b) Schematic picture for two two-level quantum emitters with dipole orientations $\vec{\mu}_1$ and $\vec{\mu}_2$, respectively, and with resonance frequency $\hbar\omega_0$ coupled each to the corresponding electric field modes $\vec{E}_0(\vec{r})$. $\vec{E}_{in}(\vec{r})$ is the additional input field.

where $\lambda = 1{,}2$ gives the two possible polarization for each mode with wave vector $\vec{k}$ and the polarization unit vectors $\vec{e}_{\vec{k},\lambda}$ spans a plane, that is orthogonal to the propagating direction given by the wave vector. So, finally we get

$$H_{em} = \sum_{\vec{k},\lambda} \hbar\omega_k a^\dagger_{\vec{k},\lambda} a_{\vec{k},\lambda} \tag{2.6}$$

describing the energy of the electromagnetic field with $a^\dagger_{\vec{k},\lambda}$, $a_{\vec{k},\lambda}$ the creation and annhiliation operators, respectively, which fulfill the canonical commutation relation $[a_{\vec{k},\lambda}, a^\dagger_{\vec{k}',\lambda'}]$ $= \delta_{\vec{k},\vec{k}'}\delta_{\vec{\lambda},\vec{\lambda}'}$ [20].

The Hamiltonian containing absorption and emission effects of a single quantum emitter in free space can then be written in the rotating-wave-approximation (RWA) as

$$H = \hbar\omega_0\sigma^\dagger\sigma + \sum_{\vec{k},\lambda} \hbar\omega_k a^\dagger_{\vec{k},\lambda} a_{\vec{k},\lambda} + \sum_{\vec{k},\lambda} \hbar g_{\vec{k},\lambda}(\sigma^\dagger a_{\vec{k},\lambda} + a^\dagger_{\vec{k},\lambda}\sigma), \tag{2.7}$$

where $\omega_k = c|k|$ is the frequency of each mode, $\omega_0 = E_e/\hbar$ is the transition resonance frequency with $E_g = 0$ and $g_{\vec{k},\lambda} = \sqrt{\frac{\omega_k}{2\hbar\epsilon_0 V}}\ \vec{e}_{\vec{k},\lambda} \cdot \vec{\mu}$ is the dipole coupling with dipole orientation $\vec{\mu}$ [20].

Now, we extend the Hamiltonian for the case of N identical emitters located at the positions $\vec{r_i}$ with index i = 1,...,N interacting with the common radiation field. For the example of two atoms as shown in Figure 2.1b, we get

$$H = \hbar\omega_0 \sum_i \sigma_i^\dagger\sigma_i + \sum_{\vec{k},\lambda} \hbar\omega_k a^\dagger_{\vec{k},\lambda} a_{\vec{k},\lambda} + \sum_{\vec{k},\lambda}\sum_i \hbar g^{(i)}_{\vec{k},\lambda}(\sigma_i^\dagger a_{\vec{k},\lambda} e^{i\vec{k}\cdot\vec{r_i}} + a^\dagger_{\vec{k},\lambda}\sigma_i e^{-i\vec{k}\cdot\vec{r_i}}), \tag{2.8}$$

where the dipole coupling strength of the i-th emitter now reads $g^{(i)}_{\vec{k},\lambda} = \sqrt{\frac{\omega_k}{2\hbar\epsilon_0 V}}\ \vec{e}_{\vec{k},\lambda} \cdot \mu_i$ [20].

To obtain an expression of the collective electric field at all times, we start from the Heisenberg equation for the annihilation operator

$$\dot{a}_{\vec{k},\lambda}(t) = -i\omega_k a_{\vec{k},\lambda} - i\sum_i g^{(i)}_{\vec{k},\lambda} e^{-i\vec{k}\cdot\vec{r_i}}\sigma_i. \tag{2.9}$$

Integrating this equation leads us to

$$a_{\vec{k},\lambda}(t) = a_{\vec{k},\lambda}(0)e^{-i\omega_k t} - i\sum_i g^{(i)}_{\vec{k},\lambda} e^{-i\vec{k}\cdot\vec{r_i}} \int_0^t dt' \sigma_i(t') e^{i\omega_k(t'-t)}. \tag{2.10}$$

This equation is problematic in the sense, that the field operators at a certain time t depend on the transition operators at all previous times t' and the time integral can not exactly be done. But, since we already used the fact in the RWA that the time-dependence of the system is encoded primarily in the resonance frequency of the emitters, such that

$$\sigma_i(t) \propto \sigma_i(0)e^{-i\omega_0 t}, \tag{2.11}$$

we can define an operator

$$s_i(t) := \sigma_i(t)e^{i\omega_0 t} \propto \sigma_i(0) \tag{2.12}$$

and therefore approximate the time integral

$$\int_0^t dt' \sigma_i(t') \approx s_i(t) \int_0^t dt' e^{-i\omega_0 t'} = \sigma_i(t) \int_0^t dt' e^{-i\omega_0 (t'-t)}, \tag{2.13}$$

which is called the Markov approximation [20]. Now, inserting Eq. 2.9 and Eq. 2.13 in the Eq. 2.5 of the free electric field gives the two terms

$$\vec{E^+}(\vec{r},t) = \vec{E^+_{in}}(\vec{r},t) + \vec{E^+_0}(\vec{r},t), \tag{2.14}$$

where

$$\vec{E^+_{in}}(\vec{r},t) = \sum_{\vec{k},\lambda} \sqrt{\frac{\hbar\omega_k}{2\epsilon_0 V}} \vec{e}_{\vec{k},\lambda} e^{i\vec{k}\cdot\vec{r}} a_{\vec{k},\lambda}(0) e^{-i(\omega_k t - \vec{k}\vec{r})} \tag{2.15}$$

describes the free evolution of the initial electric field, which we consider to be in a vacuum state, so $\langle \vec{E^+_{in}}(\vec{r},t) \rangle = 0$. Therefore we will neglect this term for the time being, even though it gives rise to quantum noise [20]. The collective field of the emitters $\vec{E^+_0}(\vec{r},t)$ after simplifying then reads

$$\vec{E^+_0}(\vec{r},t) = -i\sum_i \sum_{\vec{k},\lambda} \sqrt{\frac{\hbar\omega_k}{2\epsilon_0 V}} \vec{e}_{\vec{k},\lambda} g^{(i)}_{\vec{k},\lambda} e^{i\vec{k}\cdot(\vec{r}-\vec{r_i})} \sigma_i(t) \int_0^t dt' e^{i(\omega_k - \omega_0)(t'-t)}. \tag{2.16}$$

For a further integration of this term, we first solve the sum over polarization, where the polarization unit vectors $\vec{e}_{\vec{k},\lambda}$ and the unit wave vectors $\vec{k}$ form an orthonormal basis. Therefore

$$\sum_\lambda \vec{e}_{\vec{k},\lambda} g^{(i)}_{\vec{k},\lambda} = \sqrt{\frac{\omega_k}{2\hbar\epsilon_0 V}} \sum_\lambda (\vec{e}_{\vec{k},\lambda} \circ \vec{e}_{\vec{k},\lambda}) \cdot \vec{\mu_i} = \sqrt{\frac{\omega_k}{2\hbar\epsilon_0 V}} (\mathbf{1} - \hat{\vec{k}} \circ \hat{\vec{k}}) \cdot \vec{\mu_i}, \tag{2.17}$$

with the thee-dimensional identity matrix and the dyadic product denoted by $\circ$ [20]. Now, by taking the high density of modes into account, we rewrite the sum as an integral and also insert Eq. 2.17, such that we get for the electric field

$$\vec{E_0}^+(\vec{r},t) = -\frac{i}{2\epsilon_0(2\pi c)^3}\sum_i \sigma_i(t)\int d\omega_k d\omega_k^3 \int_0^t dt'\, e^{i(\omega_k-\omega_0)(t'-t)} \times \int d\Omega_k(\mathbf{1}-\hat{\vec{k}}\circ\hat{\vec{k}})\cdot\vec{\mu_i}e^{i\vec{k}\cdot(\vec{r}-\vec{r_i})} \tag{2.18}$$

Now we proceed with solving the integral over the angle $d\Omega_k$ by rewriting the integrand as

$$(\hat{\vec{k}}\circ\hat{\vec{k}})e^{i\vec{k}\cdot(\vec{r}-\vec{r_i})} = -\frac{1}{k^2}(\nabla_{\vec{r}}\circ\nabla_{\vec{r}})e^{i\vec{k}\cdot(\vec{r}-\vec{r_i})}. \tag{2.19}$$

and after exchanging the order of integration and derivation, the integral solution simply reads

$$\int d\Omega_k e^{i\vec{k}(\vec{r}-\vec{r_i})} = 4\pi\frac{\sin(k|\vec{r}-\vec{r_i}|)}{k|\vec{r}-\vec{r_i}|}. \tag{2.20}$$

In the last step, we solve the time integral, by making use of the Sokhotski-Plemelj formula

$$\int d\omega_k \int_0^t dt'\, e^{i(\omega_k-\omega_0)(t'-t)} = \int d\omega_k\Big(-\mathcal{P}\frac{i}{\omega_k\omega_0}+\pi\delta(\omega_k-\omega_0)\Big) \tag{2.21}$$

with $\mathcal{P}$ the Cauchy principal value. After applying standard complex contour integration, we can finally write the collective electric field of the quantum emitters as

$$\vec{E_0^+}(\vec{r},t) = -i\frac{3\hbar\Gamma_0}{4\mu}\sum_i \sigma_i(t)\Big[\underline{\vec{F}}(k_0,\vec{r}-\vec{r_i}) - i\underline{\vec{J}}(k_0,\vec{r}-\vec{r_i})\Big]\cdot\hat{\vec{\mu}}_i, \tag{2.22}$$

where

$$\underline{\vec{F}} := \Big(\frac{sin(kr)}{kr}+\frac{cos(kr)}{(kr)^2}-\frac{sin(kr)}{(kr)^3}\Big)\mathbf{1} - (\hat{\vec{r}}\circ\hat{\vec{r}})\Big(\frac{sin(kr)}{kr}+3\frac{cos(kr)}{(kr)^2}-3\frac{sin(kr)}{(kr)^3}\Big) \tag{2.23}$$

and

$$\underline{\vec{J}} := \Big(\frac{cos(kr)}{kr}-\frac{sin(kr)}{(kr)^2}-\frac{cos(kr)}{(kr)^3}\mathbf{1} - (\hat{\vec{r}}\circ\hat{\vec{r}})\Big(\frac{cos(kr)}{kr}-3\frac{sin(kr)}{(kr)^2}-3\frac{cos(kr)}{(kr)^3}\Big). \tag{2.24}$$

$\hat{\vec{r}}$ is the position unit vector, $\mu = |\vec{\mu_j}|$ and the spontaneous emission rate of a single quantum emitter $\Gamma_0 = \omega_0^3\mu^2/(3\pi c^3\epsilon_0\hbar)$ [20].

If we transcribe the electric field in terms of the Green's tensor for a oscillating dipole

$$\underline{\vec{G}}(k,\vec{r}) := e^{ikr}\Big[\Big(\frac{1}{kr}+\frac{i}{(kr)^2}-\frac{1}{(kr)^3}\Big)\mathbf{1} - (\hat{\vec{r}}\circ\hat{\vec{r}})\Big(\frac{1}{kr}+\frac{3i}{(kr)^2}-\frac{3}{(kr)^3}\Big)\Big], \tag{2.25}$$

the total electric field takes the form

$$\vec{E}^+(\vec{r},t) = \vec{E_{in}^+}(\vec{r},t) - \frac{3\hbar\Gamma_0}{4\mu}\sum_i \sigma_i(t)\underline{\vec{G}}(k_0,\vec{r}-\vec{r_i})\cdot\hat{\mu}_i. \tag{2.26}$$

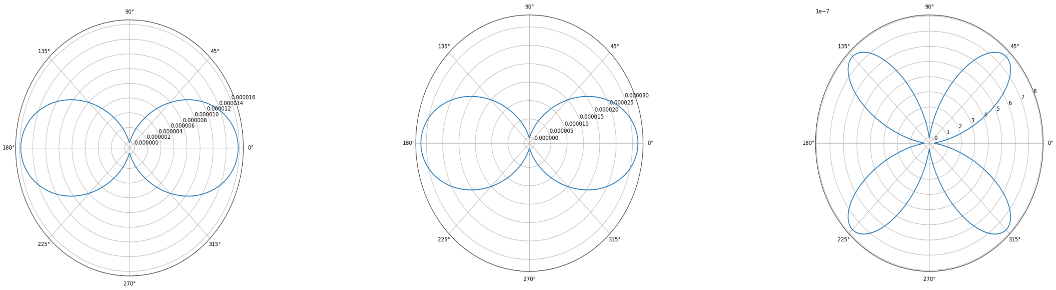

(a) $|\psi\rangle = |e\rangle$ **(b)** $|\psi\rangle = \frac{|eg\rangle+|ge\rangle}{\sqrt{2}}$ **(c)** $|\psi\rangle = \frac{|eg\rangle-|ge\rangle}{\sqrt{2}}$

Figure 2.2: *Radial radiation patterns.* - Radiated intensity of a (a) single dipole and of two coupled dipoles in a (b) superradiant and (c) subradiant state, respectively. The two quantum emitters are subwavelength-spaced with a distance d=0.1λ_0 along the axis of their dipole orientations. The intensity is calculated as a function of θ in the same plane of the dipole moment(s) around the emitter(s). The single emitter shows a weaker intensity field compared to the coupled dipole field, how expected. The subradiant intensity pattern however is a factor 1e-7 smaller.

To determine the collective radiation intensity of the quantum emitters, we can define the radiated intensity as

$$\vec{I}(\vec{r},t) := \langle \vec{E}^{-}(\vec{r},t) \cdot \vec{E}^{+}(\vec{r},t) \rangle \,, \tag{2.27}$$

which is depicted in Figure 2.2 for the case of a single and two coupled quantum emitters, respectively, in the single-excitation manifold. We can see here already the phenomena of super- and subradiance, where for superradiance the intensity is significantly larger compared to the almost zero field intensity of the subradiant mode.

2.2 Dipole-dipole Interaction

For a full description of the coherent dynamics in our system, we define the dipole Hamiltonian

$$H_{\text{dip}} = \sum_{j \neq k} \Omega_{jk} \sigma_j^{+} \sigma_k^{-} \,, \tag{2.28}$$

which provides coherent energy transfer between the quantum emitters. For this we defined the coherent coupling

$$\Omega_{ij} := -\frac{3\Gamma_0}{4} \hat{\vec{\mu}}_i \cdot \underline{\vec{J}}(k_0, \vec{r_i} - \vec{r_j}) \cdot \hat{\vec{\mu}}_j \tag{2.29}$$

as well as the collective decay rates

$$\Gamma_{ij} := \frac{3\Gamma_0}{2} \hat{\vec{\mu}}_i \cdot \underline{\vec{F}}(k_0, \vec{r_i} - \vec{r_j}) \cdot \hat{\vec{\mu}}_j . \tag{2.30}$$

In Figure 2.3 the distance dependence of the couplings Ω_{ij} and Γ_{ij} can be seen for two different dipole orientations. For the dipole orientation perpendicular to the direction of the emitters' alignment the coherent interactions for $0.2 < r_{ij} < 1$ are much stronger. Further, we can see that for $r_{ij} \to 0$, $\Omega_{ij} \to \pm\, \infty$ and $\Gamma_{ij} \to 1$, so the energy shifts will

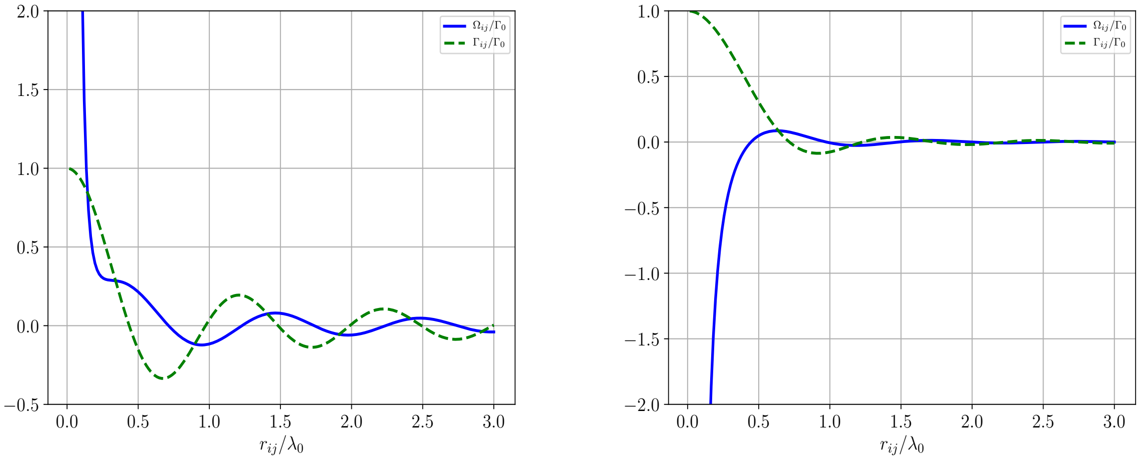

(a) tangential, $\theta = 0$

(b) transverse, $\theta = \pi/2$

Figure 2.3: *Coherent and dissipative couplings.* - Dependence of the couplings Ω_{ij} and Γ_{ij} on the distance r_{ij} in units of the single emitter spontaneous emission rate Γ_0 with $\lambda_0 = 1$ for two different dipole orientations.

diverge and the collective decay rates become the single spontaneous emission rate $\Gamma_{ij} = \Gamma_0$, respectively, which is called the Dicke Limit [3]. In this case one can reduce the Hilbert space of N two-level systems to one effective spin. For the case $r_{ij} \to \infty$, both $\Omega_{ij} \to 0$ and $\Gamma_{ij} \to 0$, which describes two-level emitters infinitely far apart from each other, so $\Gamma_{ij} = \delta_{ij}\Gamma_0$ [21].

2.3 Master Equation

To get insights to the dynamics of the ensemble of dipole-coupled quantum emitters, which includes both the collective dipole coupling as well as the collective decay of the atoms, we can use the master equation. For this, we first need to find an equation for the reduced density operator. By doing so, we start with writing down the density matrix ρ of a single quantum emitter in an arbitrary state in the basis $|e\rangle$, $|g\rangle$.

$$\rho(t) = \rho_{ee}(t)\,|e\rangle\,\langle e| + \rho_{eg}(t)\,|e\rangle\,\langle g| + \rho_{ge}(t)\,|g\rangle\,\langle e| + \rho_{gg}(t)\,|g\rangle\,\langle g|\,, \tag{2.31}$$

where ρ_{ij} are the time dependent complex matrix elements. The time evolution is given by

$$\frac{\partial\rho}{\partial t} = \dot{\rho} = i[\rho, H]. \tag{2.32}$$

To calculate the expectation value of an arbitrary operator A(t), we use

$$\langle A\rangle\,(t) = \mathrm{tr}(A(t)\rho) = tr(A\rho(t)). \tag{2.33}$$

By taking the time derivative, we have

$$\mathrm{tr}(\dot{A}\rho) = \mathrm{tr}(A\dot{\rho}) \tag{2.34}$$

If we insert the Quantum Langevin equation for the arbitrary operator A at this point we get: [20]

$$\dot{A} = \frac{i}{\hbar}[H_0 + H_{\text{dip}}, A] + \sum_{j,k}[\sigma_j^\dagger, A]\Big(\delta_{jk}\sqrt{\Gamma}\xi_j(t) + \frac{\Gamma_{jk}}{2}\sigma_k\Big) - \sum_{j,k}\Big(\delta_{jk}\sqrt{\Gamma_0}\xi_j^\dagger(t) + \frac{\Gamma_{jk}}{2}\sigma_k^\dagger\Big)[\sigma_j, A] \tag{2.35}$$

with the quantum noise operator

$$\xi_j(t) := \frac{i}{\hbar\sqrt{\Gamma_0}}\Big(\vec{\mu}_j \cdot \vec{E}_{in}^+(\vec{r}_j, t)\Big). \tag{2.36}$$

For Eq. 2.34 we then get

$$\text{tr}(\dot{A}\rho) = \text{tr}\Bigg[A\Big(-\frac{i}{\hbar}[H_0 + H_{\text{dip}}, \rho] + \sum_{j,k}\frac{\Gamma_{jk}}{2}(2\sigma_j\rho\sigma_k^\dagger - \sigma_j^\dagger\sigma_k\rho - \rho\sigma_j^\dagger\sigma_k)\Big)\Bigg]. \tag{2.37}$$

Comparison with Eq. 2.34 finally gives the master equation

$$\dot{\rho} = -\frac{i}{\hbar}[H_0 + H_{\text{dip}}, \rho] + \mathcal{L}[\rho], \tag{2.38}$$

where

$$\mathcal{L}[\rho] := \sum_{j,k}\frac{\Gamma_{jk}}{2}(2\sigma_j\rho\sigma_k^\dagger - \sigma_j^\dagger\sigma_k\rho - \rho\sigma_j^\dagger\sigma_k)\Big) \tag{2.39}$$

is the so-called Liouville operator written above in the standard Linblad form, which accounts for the dissipation in the system [20].

2.4 The System

Now we use the previous findings to concretise our model in the following sections. For the sake of clarity, we split this section up into two parts, the description of a single ring and of coupled rings, respectively.

2.4.1 Single Ring

We consider N identical two-level quantum emitters with given dipole orientations, which are uniformly located on a regular ring (polygon) with a distance d to each other, as depicted in Figure 2.4.

After integrating out the photonic degrees of freedom, the internal dynamics in the Born-Markov-Approximation are described by the master equation $\dot{\rho} = -i[H_{\text{dip}}, \rho] + \mathcal{L}[\rho]$, where the Hamiltonian, written in a frame rotating at the atomic transition frequency ω_0, corresponds to Eq. 2.28 with the Lindblad operator Eq. 2.39. The collective energy shifts can be written as

$$\Omega_{ij} = -\frac{3\pi\Gamma_0}{k_0}\Re\{\hat{\vec{\mu}}_i^* \cdot \vec{G}(\vec{r}_i - \vec{r}_j, \omega_0) \cdot \hat{\vec{\mu}}_j\} \tag{2.40}$$

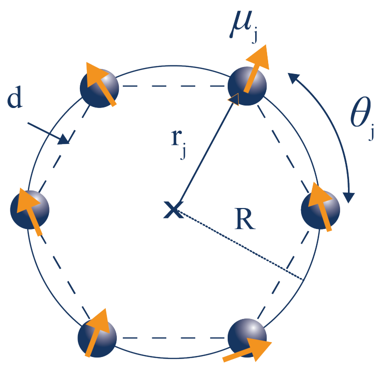

Figure 2.4: Ring of subwavelength-spaced quantum emitters with inter-particle distance d, given dipole orientation $\hat{\mu}_i$ and angle θ_j associated with the site j

and the collective decay rates read

$$\Gamma ij = \frac{6\pi\Gamma_0}{k_0}\Im\{\hat{\vec{\mu}}_i^* \cdot \vec{G}(\vec{r_i} - \vec{r_j}, \omega_0) \cdot \hat{\vec{\mu}}_j\}. \tag{2.41}$$

The Green's tensor in free space acting on a oscillating unit dipole $\hat{\vec{\mu}}$ can be written as

$$\vec{G}(\vec{r}, \omega_0) \cdot \hat{\vec{\mu}} = \frac{e^{ik_0 r}}{4\pi r}\left[(\hat{\vec{r}} \times \hat{\vec{\mu}}) \times \hat{\vec{r}} + \left(\frac{1}{k_0^2 r^2} - \frac{i}{k_0 r}\right)(3\hat{\vec{r}}(\hat{\vec{r}} \cdot \hat{\vec{\mu}} - \hat{\vec{\mu}})\right], \tag{2.42}$$

with the unit position vector $\hat{\vec{r}}$ and the atomic transition wavenumber $k_0 = \omega_0/\mathrm{c}$. The electric field then reads [13]

$$\vec{E}^+(\vec{r}) = \frac{\mu k_0^2}{\epsilon_0}\sum_i \vec{G}(\vec{r} - \vec{r}_i, \omega_0) \cdot \hat{\vec{\mu}}_i \cdot \sigma_i^-. \tag{2.43}$$

Since describing an ensemble of two-level quantum emitters is mathematically equivalent to describing spin-1/2-particles, the eigenbasis of the Hamiltonian can be divided into subsets of different excitation numbers and the corresponding states form a basis in that very subspace. So, for the purpose of simplicity we restrict our Hamiltonian to the single-excitation manifold. Note, that the analytical form of the basis states in the mentioned subspaces can only be approximated. But since we are only interested in the generated fields and excited state populations, respectively, we are allowed to neglect the so-called recycling term in the Linblad operator, which only is the book keeper of the ground state population and does not modify the observables of interest. Therefore we can understand our system by investigating the effective, but non-hermitian Hamiltonian [13]

$$H_{\text{eff}} = \sum_{i,j}(\Omega_{ij} - i\frac{\Gamma_{ij}}{2}\sigma_i^+\sigma_j^-). \tag{2.44}$$

The eigenstates of H_{eff} provide a set of collective modes and the associated complex eigenvalues gives us the collective frequency shifts as well as the collective decay rates by taking the real and imaginary part, respectively. If we further assume the dipole orientations to be rotational invariant, the collective modes become perfect spin waves [13]

$$|\psi_m\rangle = \frac{1}{\sqrt{N}}\sum_{j=1}^{N} e^{im\theta_j}|e_j\rangle, \tag{2.45}$$

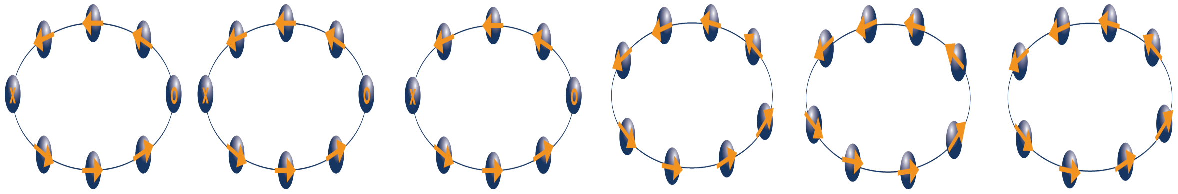

(a) Site-site-configuration **(b)** Site-edge-configuration **(c)** Edge-edge-configuratiion

Figure 2.5: *Coupled rings.* - Schematics of two single rings of subwavelength-spaced quantum emitters with inter-particle distance d separated by the distance x for different configurations.

where N is the number of quantum emitters, m = 0, ± 1, ± 2, ..., ⌊ ± (N-1)/2 ⌋ the angular momentum of the mode and $\theta_j = 2\pi(j-1)/N$ the angle to the site index j = 1, ..., N of the atom of concern. The state $|e_j\rangle = \sigma_j^+ |g\rangle$ means that only the atom at site j is excited, so the excitation is completely delocalized over all sites. The eigenvalues of H_{eff} are

$$\lambda_m = -\frac{3\pi\Gamma_0}{Nk_0}\sum_{j,k} e^{im(\theta_l-\theta_j)}G_{jl}, \tag{2.46}$$

where $G_{jl} = \hat{\vec{\mu}}_j^* \cdot \vec{G}(\vec{r}_j - \vec{r}_l, \omega_0) \cdot \hat{\vec{\mu}}_l$. With this we can calculate the collective frequency shifts and the collective decay rates, respectively,

- $J_m = \Re\{\lambda_m\}$
- $\Gamma_m = -2\Im\{\lambda_m\}$

Note, that the spectrum is symmetric, so $\lambda_m = \lambda_{-m}$, whereas the mode m = 0 is non-degenerate, but the maximum valued modes are doubly-degenerate if the number of emitters N is even and therefore we have just one effective mode.

2.4.2 Two coupled Rings

In this section, we describe two coupled rings in the same plane separated by a distance x as depicted in Fig. 2.5. Note, that there are several possible generic configurations, shown in Figure 2.5a - 2.5c.

The effective Hamiltonian can be split up in the sum of intra-ring as well as ring-ring coupling terms

$$H_{\text{eff}} = \sum_{i,j\in R_1} h_{i,j} + \sum_{i,j\in R_2} h_{i,j} + \sum_{i\in R_1, j\in R_2} h_{i,j}, \tag{2.47}$$

where $h_{i,j} = -(3\pi\Gamma_0/k_0)G_{ij}$ and $R_1 = \{1, 2, ..., N\}$ denotes the set of indexes of the first ring and $R_2 = \{N+1, ..., 2N\}$ denotes the set of indexes of the second ring, respectively [13]. The last term expresses the coupling between the rings, which is important to us here. We can write it in the angular momentum basis as [13]

$$\sum_{i\in R_1, j\in R_2} h_{i,j} = \sum_{m_1,m_2} (J_{m_1,m_2} - i\Gamma_{m_1,m_2}/2)\sigma_{m_1,1}^+ \sigma_{m_2,2}^-, \tag{2.48}$$

where $J_{m_1,m_2} = \Re\{\lambda_{m_1 m_2}\}$ is again the dispersive coupling and $\Gamma_{m_1,m_2} = -2\Im\{\lambda_{m_1,m_2}\}$ the dissipative coupling, with the eigenvalues

$$\lambda_{m_1,m_2} = \frac{1}{N} \sum_{i\in R_1, j\in R_2} h_{i,j} e^{i(m_1\theta_i - m_2\theta_j)}. \tag{2.49}$$

To get an expression for the coupling efficiency, we calculate the ratio

$$\eta_{m_1,m_2} = \frac{J^2_{m_1,m_2}}{(4\Delta^2_{m_1,m_2} + \max\{\Gamma^2_{m_1}, \Gamma^2_{m_2}\})}, \tag{2.50}$$

where $\Delta^2_{m_1,m_2} = |J_{m_1} - J_{m_2}|$ [13].

With this we can evaluate how good two modes in the two rings are coupled and how efficient an excitation transfer is. This leads to the question, how we can model a efficient excitation transfer between two rings. First it is to mention, that a fully delocalized excitation as we have considered so far does not reflect a typical case, since excitations occur partially localized. To take this into account, we construct a multi-mode Gaussian wave-packet centered at the site k in the i-th ring

$$|\Psi^m_{i,k}\rangle = \frac{1}{\sqrt{n}} \sum_{j\in R_i} e^{i\theta_j m} e^{-\frac{|\vec{r}_j - \vec{r}_k|}{2R^2\Delta\theta^2}} |e_j\rangle\,, \tag{2.51}$$

where n accounts for the normalization, $\Delta\theta$ denotes the angular spread of the wave-packet with width $R\Delta\theta$, and m is the central momentum [13]. By taking an infinitely wide wave-packet $\Delta\theta > 2\pi$, we reduce Eq. 2.51 to an eigenstate of our system with the corresponding angular momentum m. A schematic is shown in Figure 2.6.

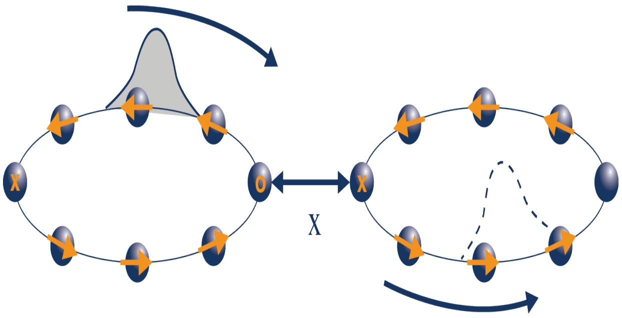

Figure 2.6: Partially localized single excitation is transferred between two rings separated by a distance x in site-site-configuration.

For a guided mode in the first ring with momentum m, we expect that, while the mode is transported to the second ring, it will invert its momentum. So, for the finite width wave-packet we can assume, that it is transferred nearly unaffected to the second ring, whereby the central momentum inverts to -m. With this assumption we can analyze the fidelity $\mathcal{F}$ of creating this wave-packet in the second ring as follows

$$\mathcal{F}(t) = \max_k \Big\{ \langle \Psi^{-m}_{2,k} | \Psi(t) \rangle \Big\}, \tag{2.52}$$

where $|\Psi(t)\rangle$ is given by the unitary time evolution with the effective Hamiltonian and the initial condition $|\Psi(0)\rangle = |\Psi^m_{1,k}\rangle$ and the maximization over the site k is due to the fact that we can not predict the position of the wave-packet created there at all times [13].

3 Single Ring: Collective Excitations and radiative Properties

In this chapter we provide a full examination of the collective properties of the single ring excitons. In order to do so, we use the insights presented in section 2.4.1. We will first discuss the collective decay rates and frequency shifts in dependence of different parameters and will then analyze the radiative properties.

3.1 Collective Dynamics - Single-Excitation Manifold

In the following we study the collective dynamics for different modes and polarizations for the single-excitation manifold first and second for the two-excitation manifold. We also provide insights in the decay of such a system starting in a super- as well as subradiant state. Finally, we add a driving laser into the systems' Hamiltonian and investigate its effects onto the decay.

3.1.1 Geometrical Properties

Starting with transverse polarization (Figure 3.1), we can see, that by decreasing the inter-particle distance d, one bright mode emerges for m = 0, as well as N-1 dark modes as depicted in Figure 3.1a. In this case the emitters are so close, that the range of interaction is effectively infinite. This is called the "Dicke limit" [3]. The maximal decay increases linearly at a rate $\Gamma = N\Gamma_0$ as we would expect and as already mentioned in section 2.2, depicted in Figure 3.1c.

In the case of tangential polarizations for a ring of N = 8 emitters (Figure 3.1) we get two bright modes for m = ±1, depicted in Figure 3.1b. The decay rate is close to $\Gamma = \frac{N\Gamma_0}{2}$, depicted in Figure 3.1d. In both cases the collective decay rate Γ_m becomes the single emitter spontaneous emission rate Γ_0, if the inter-particle distance is big enough and the collective effects are negligible.

Note that the range of the frequency shifts of the collective modes gets larger by increasing the density of the ring of constant size. The dipole orientations determine, whether the bright or the dark modes are higher in energy (Figure 3.2). If the polarization vectors are oriented transversely (Figure 3.2a), the bright modes are higher in energy, contrary to the tangential case (Figure 3.2b), where the bright modes are lower in energy.

Now we analyze the behavior of the collective decay rates depending on the dipole orientation ϕ for a ring with N = 8 emitters again, like shown in Figure 3.3. For this we start rotating the polarization initially tangentially oriented upwards to transverse polarizations. Here the superradiant mode m = 0 first increases and the modes m = ± 1 then decrease

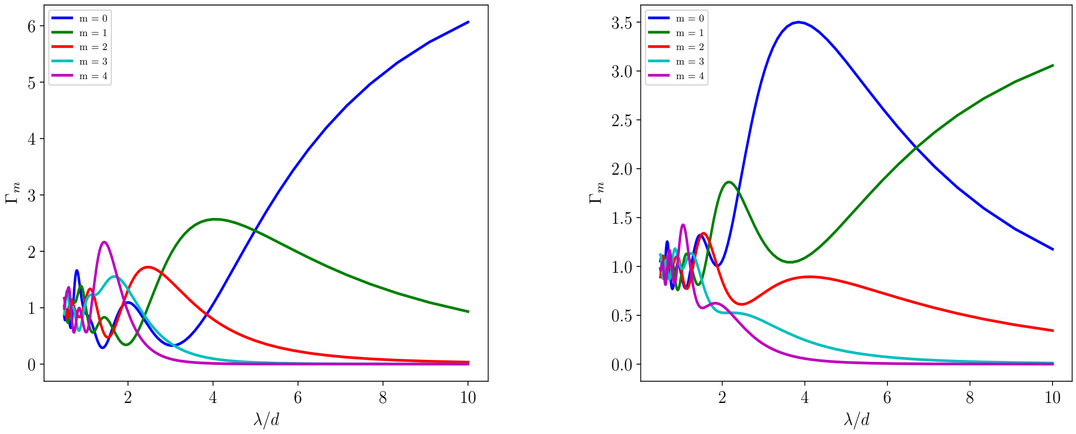

(a) Γ_m of the different modes m in units of Γ_0 as a function of λ/d with N = 8 emitters. A single bright mode m = 0 occurs in the Dicke Limit $\lambda/d \to \infty$ as well as N-1 dark modes.

(b) Γ_m of the different modes m in units of Γ_0 as a function of λ/d with N = 8 emitters. Two bright modes m = ± 1 occur in the Dicke Limit $\lambda/d \to \infty$, while m = 0 is dark by symmetry.

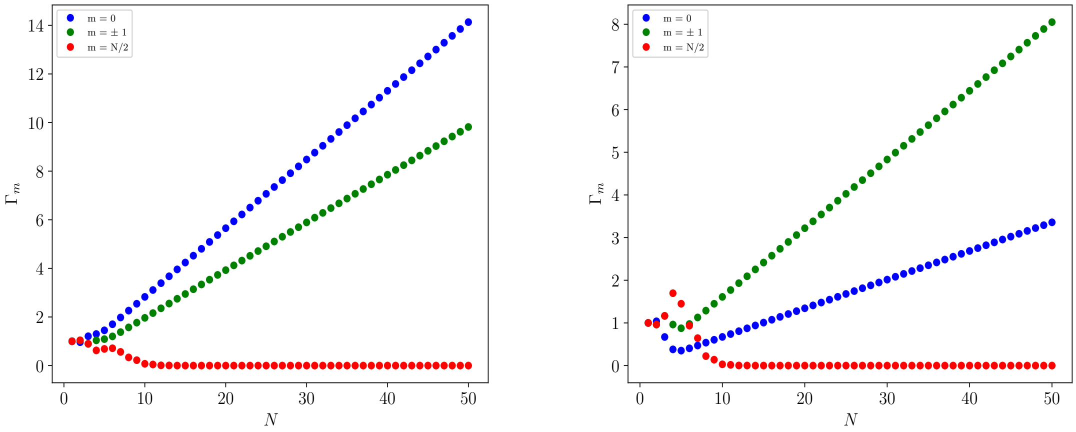

(c) Γ_m of the different modes m in units of Γ_0 as a function of the number of emitters N with fixed radius R = 0.5λ (increasing the density of the ring with constant size). The bright mode scales linearly with $\Gamma \approx N\Gamma_0$.

(d) Γ_m of the different modes m in units of Γ_0 as a function of the number of emitters N with fixed radius R = 0.5λ (increasing the density of the ring with constant size). The bright modes scale linearly with $\Gamma \approx \frac{N\Gamma_0}{2}$.

Figure 3.1: *Single ring collective decay rates in the single-excitation manifold.* The left side shows the simulations for transverse polarizations, the right side for tangential polarizations.

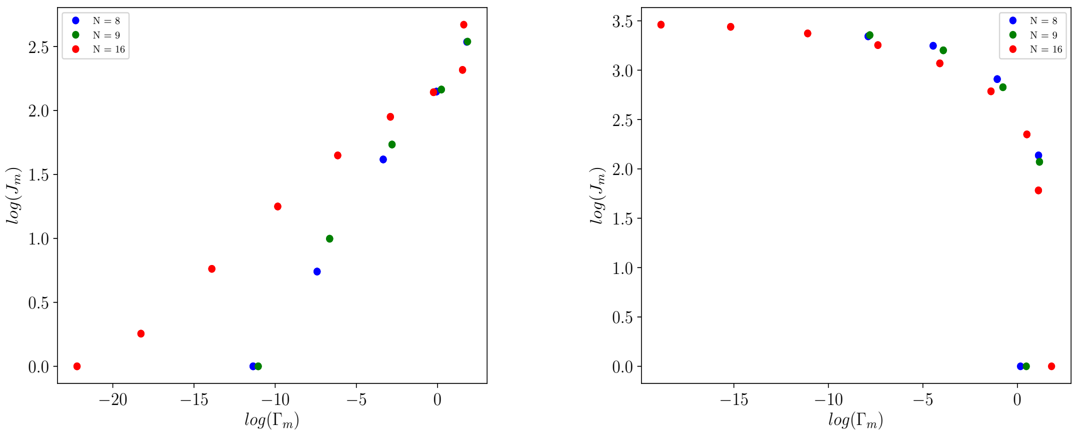

(a) Energy log-log-plot for transverse polarizations.

(b) Energy log-log-plot for tangential polarizations.

Figure 3.2: *Single ring energy in the single-excitation manifold with inter-particle distance $d = 0.1$ for different N for transverse and tangential polarizations, respectively.*

exponentially in reverse order. The most subradiant states m = 3, 4 do not change their behavior, while m = 2 becomes also subradiant. But, as we can see in the logplot Figure 3.3b for m = 3, 4 the collective decay rates decrease exponentially for transverse polarization. Starting with tangential polarizations the energy shifts J_m change their sign and the amplitude shrinks significantly, shown in Figure 3.3c.

Finally, to get a better viewpoint, we plot the collective decay rates as function of the dipole orientations for different modes and inter-particle-distances, which is shown in Figure 3.4. In summary, we observe, that for transverse polarization the lowest modes (in absolute values) and smallest distances ensure the best superradiance, while the N/2-modes and smallest distances provide the best subradiance behavior unattached by the dipole orientation. Comparing tangential and transverse polarization we notice, that transverse polarization offer the strongest collective effects in super- as well as subradiance conduct.

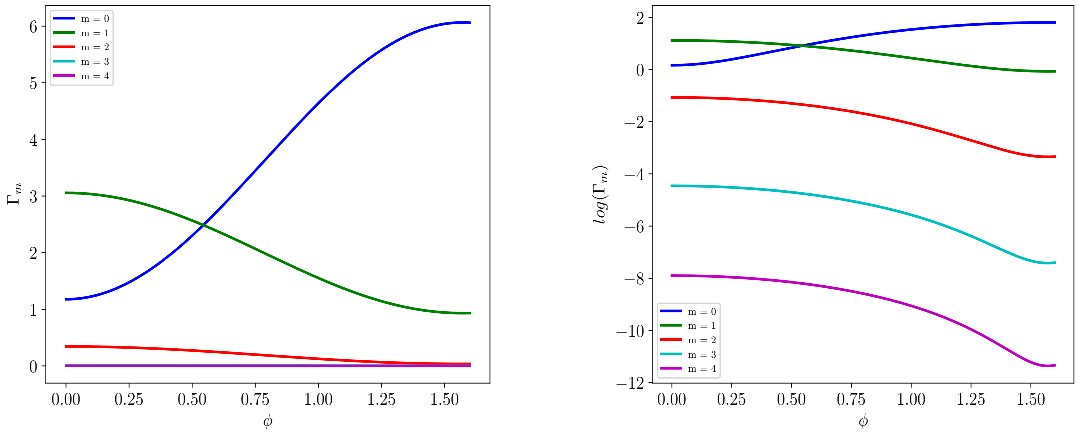

(a) Γ_m of the different modes m in units of Γ_0 as a function of the dipole orientation ϕ. Two bright modes m $= \pm$ 1 occur for $\phi = 0$, while m $= 0$ is getting dominant with increasing ϕ and is strongest for transverse polarization, as expected.

(b) Same as (a), but depicted in a log-plot. We can see, that the behavior is partially exponential.

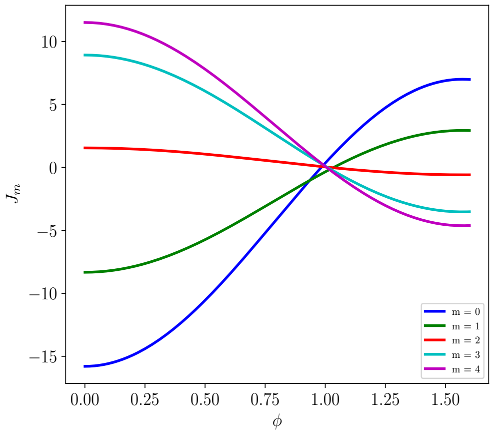

(c) Energy shifts J_m. The amplitude of the energy shifts become much lower towards transverse polarization and changes the sign around roughly $\pi/3$.

Figure 3.3: *Single ring collective decay rates Γ_m and energy shifts J_m in the single-excitation manifold as a function of the dipole polarization for $N = 8$ and $d = 0.1$.*

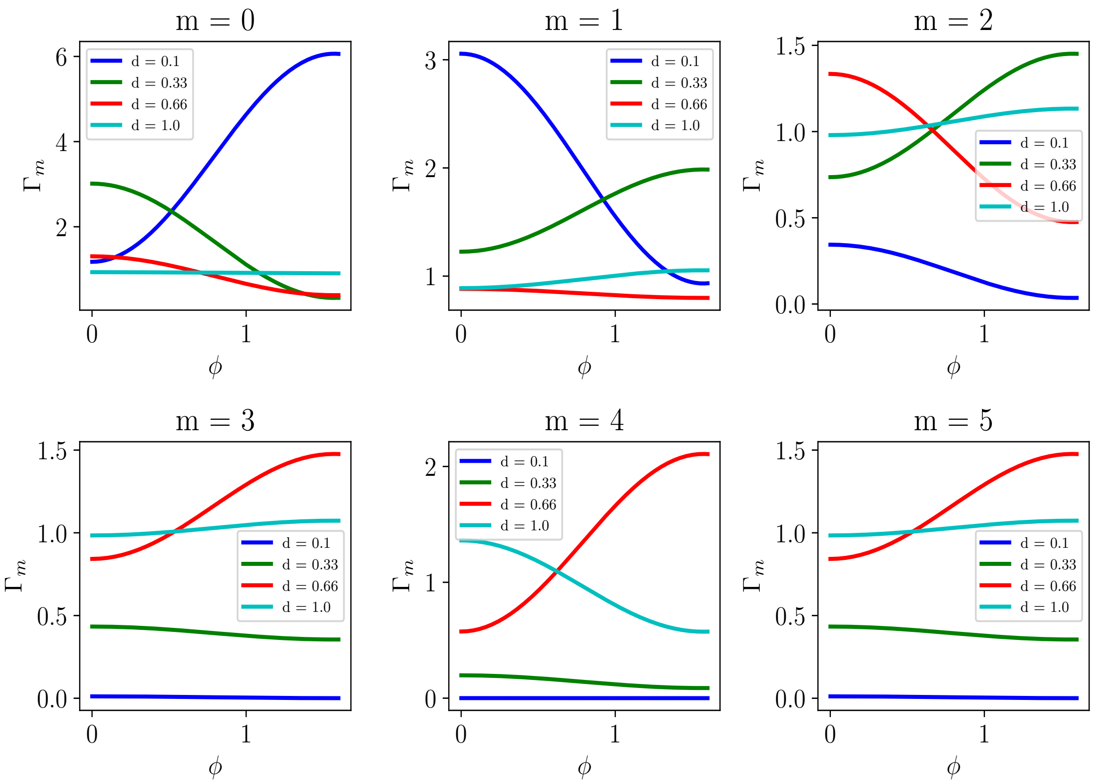

Figure 3.4: Γ_m of the different modes m in units of Γ_0 as a function of the dipole orientations ϕ with N = 8 emitters. The higher the mode m and smaller the inter-particle distance d, the more subradiant the system is and vice versa for modes m = 0, ± 1.

3.1.2 Decay from a superradiant as well as subradiant State

In Figure 3.5 the population decay as function of time of the subradiant eigenstates of the system for a ring and a chain of quantum emitters are plotted. For the ring configuration we can confirm, that the modes m = 0 and m = 1 describe the most superradiant states for transverse and tangential polarization, respectively. The mode m = N/2 is obviously the most subradiant state in both cases (Figure 3.5a and 3.5b). Note, that the timescales for the subradiant plots are a factor 40 longer than used for the superradiant plots. Even in this huge time range, we observe, that the most subradiant state does barely decay at all, especially for transverse polarization.

In Figure 3.5c and 3.5d the same simulations are shown for a chain of subwavelength-spaced two-level quantum emitters in the single-excitation manifold. Out of this it is apparent, that closing the chain by forming a ring goes along with dramatically enhancing the lifetime of the most subradiant states. Contrary to that, the superradiant states for the ring configuration show a slightly increased decay rate, especially once again for transverse polarization (Figure 3.6).

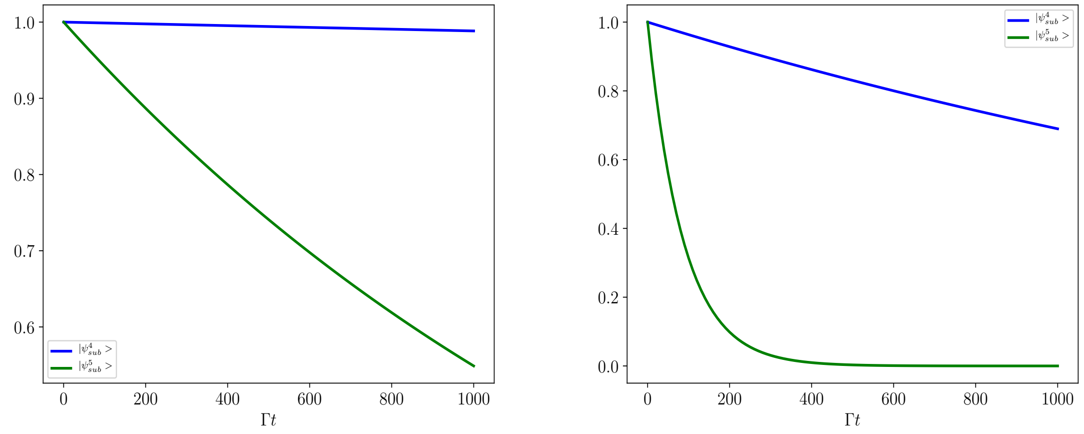

(a) Transverse polarization in a single ring.

(b) Tangential polarization in a single ring.

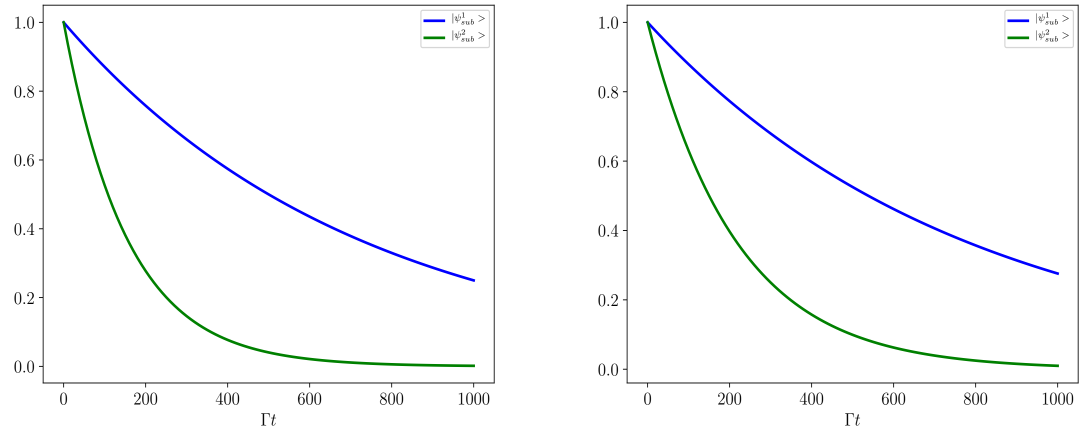

(c) Transverse polarization in a chain.

(d) Tangential polarization in a chain.

Figure 3.5: *Decay from subradiant states in a ring (a-b) and a chain (c-d) of quantum emitters.* - Population decay for a single ring with N = 8, inter-particle distance d = 0.1 and transverse polarization (left) and tangential polarization (right), respectively. Γ is the single emitter spontaneous emission rate. The upper indexes describe the modes m for the ring configuration, the most subradiant state for the chain configuration is denoted with index 1.

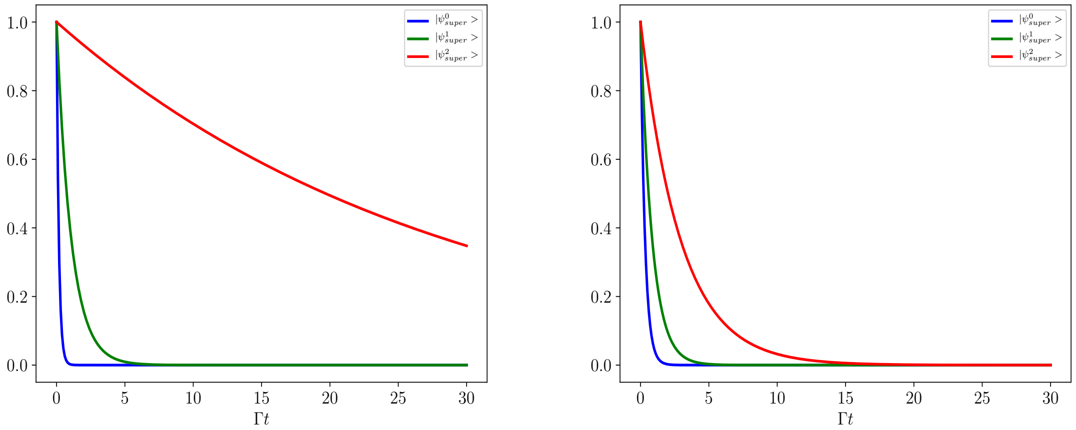

(a) Transverse polarization in a single ring.

(b) Tangential polarization in a single ring.

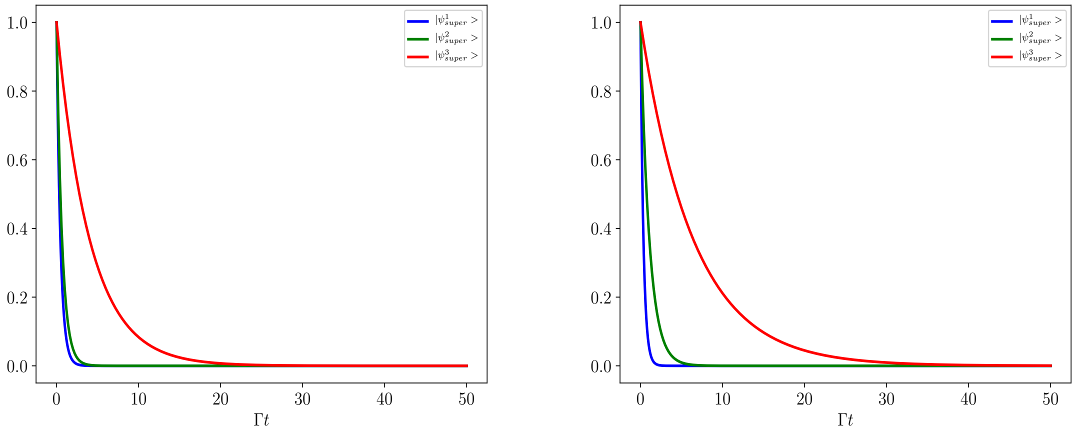

(c) Transverse polarization in a chain.

(d) Tangential polarization in a chain.

Figure 3.6: *Decay from superradiant states in a ring (a-b) and a chain (c-d) of quantum emitters.* - Population decay for a ring and a chain of two-level atoms with N = 8, inter-particle distance d = 0.1 and transverse polarization (left) and tangential polarization (right), respectively. Γ is the single emitter spontaneous emission rate. The upper indexes describe the modes m for the ring configuration, the most superradiant state is denoted with index 1 for the chain configuration.

Disorder

As the ring positions in an experiment will not be perfect, we want to study the impact of positioning disorder on the properties of the subradiant states. For this we include an uncertainty in the position of each emitter, where we allow only for radial disorder, disorder in z-direction perpendicular to the xy-plane and a overall disordering in all directions. We again diagonalize the effective Hamiltonian and average over 100 random configurations in order to find the mean minimum decay channel and the most subradiant state, respectively. We then prepare the system in that very state and let it evolve freely. The results are plotted in Figure 3.7. As we could see frequently before, the subradiant state for small enough inter-particle distances is extremely stable in the given ring configuration. If we disorder now the positions, we can observe, that this stability drops massively and the considered state decays several orders of magnitude faster (Figure 3.7a, 3.7b). As opposed to that, for larger inter-particle distances, where the subradiant state regarding the decay is not that steady, we can attain a remarkable stabilization of the state if we strongly disorder the atoms on the ring by concurrently maintaining the ring symmetry (Figure 3.7c). The effect increases with increasing disorder in the system, such that we can even construct a more stable subradiant state on the whole time scale if we radially disorder the positions of the emitters (Figure 3.7d).

Finally, we analyze the stability of the subradiance, whereas we randomize the dipole orientations, and every orientation between tangential and transverse is possible. Once more, we average over 100 random configurations and plot the corresponding decay rate, depicted in Figure 3.8. Due to the broken symmetry, we can observe, that for d = 0.1 the state is forced again into a highly faster decaying channel (Figure 3.8a). For d = 0.4 the state on short time scales also decays faster, but on larger time scales we notice again, that we can reach a slower decaying channel by disordering the system (Figure 3.8b).

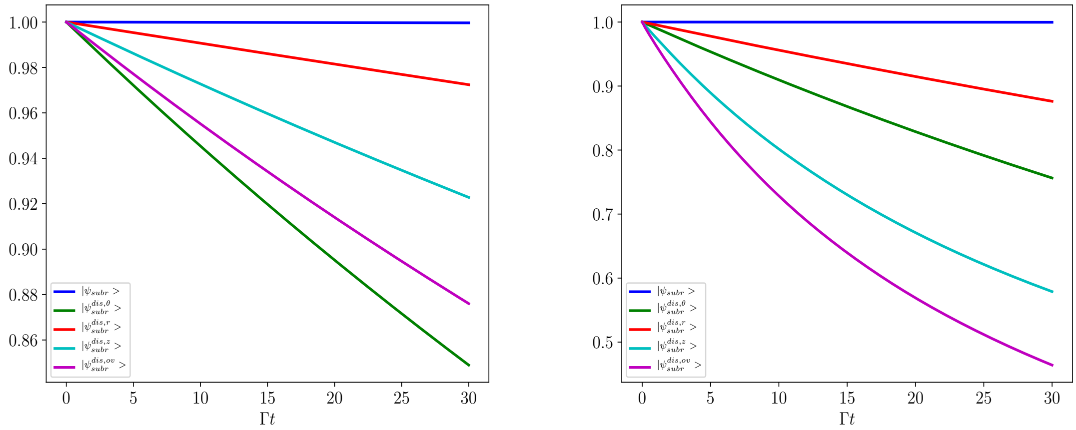

(a) d = 0.1, s = ± 20 % **(b)** d = 0.1, s = ± 40 %

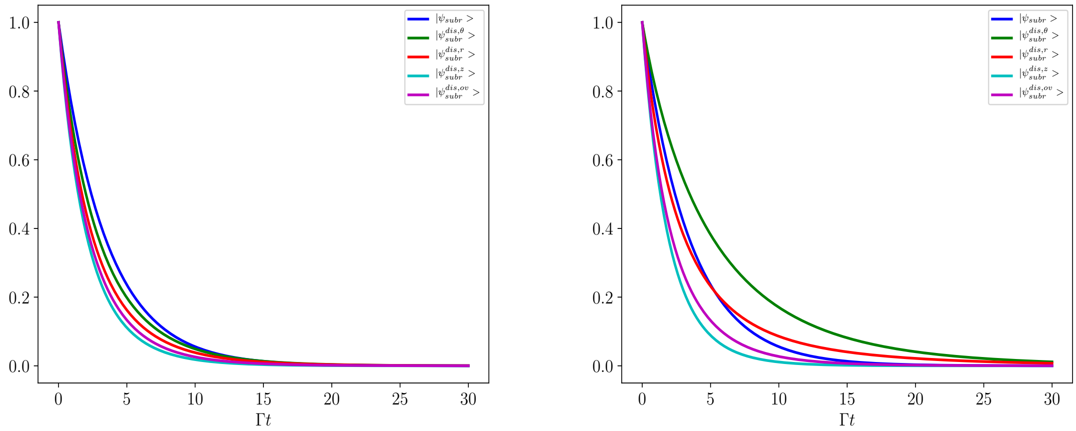

(c) d = 0.4, s = ± 20 % **(d)** d = 0.4, s = ± 40 %

Figure 3.7: *Subradiance in a disordered system.* - Subradiant state population in a ring of disordered emitter positions with N = 8 for transverse polarization and different inter-particle distances. The disorder parameter s denotes the range of disorder of the unperturbed emitter position in percentage. The subindexes denotes the kind of disorder, whereas $|\psi_{subr}\rangle$ is the undisordered subradiant state.

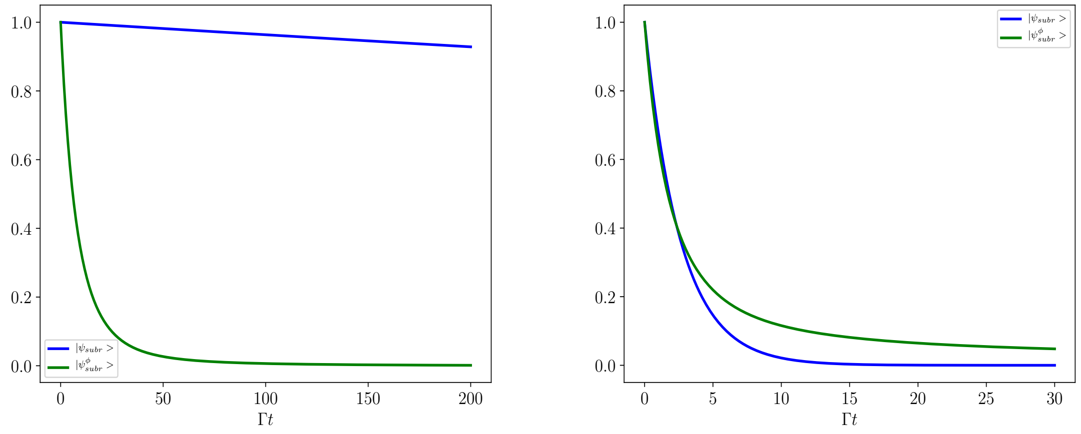

(a) d = 0.1 **(b)** d = 0.4

Figure 3.8: *Subradiance in a disordered system.* - Subradiant state population in a ring of disordered emitter positions with N = 8 for randomized polarization and different inter-particle distances. The subindex denotes the kind of disorder, whereas $|\psi_{subr}\rangle$ is the undisordered subradiant state.

3.1.3 State preparation

As we could see before, the most subradiant states in a single ring of two-level quantum emitters in the single-excitation manifold posses an extraordinary long lifetime. This can be used for spectroscopy, precision measurements as well as information storage in a quantum computer for example. But for any precise measurement the particle dynamics has to be externally prepared and controlled, where we have to deal with particle-particle interactions, which in our regime here are dominated by dipole-dipole couplings, therefore dipole-dipole induced energy shifts as well as collective decays. Since the collective decay for subradiant states is mostly suppressed, it is intriguing to know, how efficiently we can prepare such a subradiant state in a single ring, starting in the ground state and driving it coherently with a laser. We can achieve such a drive by making use of the induced energy shifts in order to resonantly address the state and by imprinting an artificial, coordinated phase. Finally, we let the system evolve freely by defining a pump strength η(t) as a function of time.

But first of all, we start with a setup, in which we drive the state with the lowest decay rate with a artificial phase. The driving scheme reads

$$H_{\text{drive}}(t) = \sum_{j=1}^{N} (\eta_j \sigma_j^+ e^{-i\frac{\omega_L t}{2}} + \eta_j^* \sigma_j^- e^{i\frac{\omega_L t}{2}}), \tag{3.1}$$

where ω_L is the frequency of the laser and $\eta_j := \eta e^{-i\phi_j}$ defines the strength of the pump with which the atom j is driven with an arbitrary phase ϕ_j at first [22]. Therefore our total Hamiltonian reads

$$H(t) = H_0 + H_{\text{dip}} + H_{\text{drive}}(t). \tag{3.2}$$

In order to get rid of the time dependence, we transform into the interaction picture and get

$$H = \frac{\Delta}{2}\sum_{i=1}^{N}\sigma_z^i + \sum_{i\neq j}\Omega_{i,j}\sigma_i^+\sigma_j^- + \sum_{j=1}^{N}(\eta_j\sigma_j^+ + \eta_j^*\sigma_j^-). \tag{3.3}$$

Here $\Delta = \omega_0 - \omega_L$ denotes the detuning of the laser to the transition frequency ω_0 with the laser frequency ω_L. Now we finally want to address the most subradiant state of our system, which is also the state with minimal symmetry. To do so, we need to adjust the phases to achieve a high efficiency of the driving and address the current states. For this purpose, we just consider the phases we already used so far in the spin-wave composition to be the phases of our choice,

$$\phi_j = i\cdot m\cdot\theta_j = i\cdot m\cdot 2\pi(j-1)/N, \tag{3.4}$$

where for the angular momentum m we choose the most subradiant mode m = N/2, such that

$$\phi_j = i\pi(j-1). \tag{3.5}$$

Hence, the driving Hamiltonian becomes

$$H_{\text{drive}} = \eta\sum_j(\sigma_j^+e^{-i\pi(j-1)} + \sigma_j^-e^{i\pi(j-1)}). \tag{3.6}$$

Note, that we are considering here transverse pumping only. This is, because longitudinal pumping would require an additional phase shift. This in turn, in order to become resonant, would require a certain inter-particle distance, that would not result in a sufficient energy shift, since the states energetically would not be separated well enough because of the dipole-dipole coupling. Despite that, the question arises how to choose the detuning right in the case of transverse pumping.

Since the dipole-dipole interaction provokes energy shifts, embedded into Ω(i,j), the primary strong degeneracy gets lifted exponentially when reducing the inter-particle distance (Figure 2.3). Therefore, we have to place the quantum emitters in close vicinity to each other in order to achieve sufficient energy shifts and lifted degeneracies, such that we can address the states of interest in a reliable way, whereby the energy shifts can be calculated as

$$\Delta\omega = \langle\psi\,|\,H_{\text{dip}}\,|\,\psi\rangle\,. \tag{3.7}$$

In Figure 3.9 we show, that the most subradiant state carries also the most negative dipole shift for sufficient small inter-particle distances. For an odd number of emitters, the energy shifts are lifted up, so the coupling is slightly weaker then for an even number of emitters and therefore the decay rate enhances (see Figure 3.16 in Section 3.3). An explanation could be, that for an odd number of emitters, the symmetry of the system is imperfect with respect to the nearest-neighbour coupling. If we increase the distance between the emitters, we can see in Figure 3.9b that the order gets destroyed, in particular for N = 5, 6, 7. The overall coupling is much weaker and therefore the decay rate much bigger. As already mentioned, we can tune the magnitude of the coupling by varying the inter-particle distance. Hence, for a bigger distance it is much less probable to address the subradiant states in full, especially over a long term (saturation). In summary, the detuning Δ has to be equal to the transition frequency of the subradiant state, but with

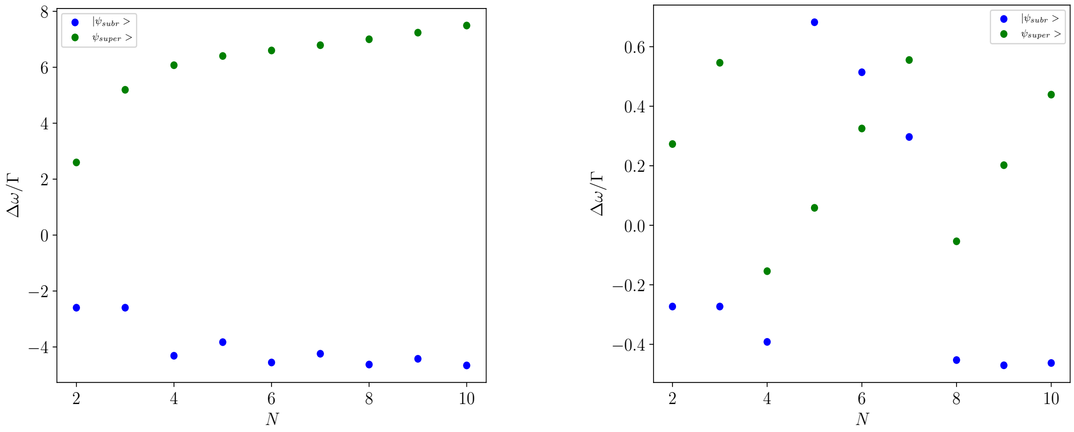

(a) d = 0.1

(b) d = 0.4

Figure 3.9: *Dipole shifts.* - Dipole-shifts for a single ring for different inter-particle distances d. The shifts are shown for the most superradiant as well as most subradiant states as function of the number of emitters N. The subradiant states are shifted maximal negatively, while the superradiant states with the highest symmetry are maximally positively shifted. Increasing the distance between the emitters destroys this order.

the addition that the dipole shift must be included, whereby the inter-particle distance has to be small enough to get a sufficient coupling strength. For the frequency of the driving laser we get $\omega_L = \omega_0 + \Delta\omega_{\text{subr}}$ and hence for the detuning

$$\Delta = \omega_0 - \omega_L = -\Delta\omega_{\text{subr}} = \langle \psi_{\text{subr}} \,|\, H_{\text{dip}} \,|\, \psi_{\text{subr}} \rangle \,. \tag{3.8}$$

In Figure 3.10 we can observe, that the chosen artificial phase works very well. Here we can see almost perfect Rabi oscillations between the ground state and the subradiant state. Since we are dealing with a two-level system, we would expect that the driven system after a long enough time reaches a steady state, where the ground state population as well as the subradiant state population is 1/2. In Figure 3.10d we can observe such a process, but interestingly, for the case of a small inter-particle distance d = 0.1 in Figure 3.10c, the system performs Rabi oscillations without any population loss in the subradiant state in favor of the ground state for a very long time. This is because for a sufficiently small inter-particle distance the decay rates for the subradiant modes become, as we already demonstrated, extremely small, and therefore the system reaches the steady state much slower. We can reach a similar effect by increasing the number of emitters on the ring, shown in Figure 3.11

Note, that increasing the number of emitters in an experiment makes the procedure far more difficult due to more potential long-range interactions, which have to be taken into account and addressed individually.

In a next step, we are interested in driving the system for a short time and let it evolve freely then. Therefore we have to define a time dependent pump strength

$$\eta(t) = \eta_0(\theta(\tau - t) - \theta(t)), \tag{3.9}$$

where $\theta(t)$ is the Heaviside function. This is illustrated in Figure 3.12. The results are depicted in Figure 3.13. For a small enough distance between the emitters we reach a almost perfect subradiant state after applying an effective π-pulse, such that there is not

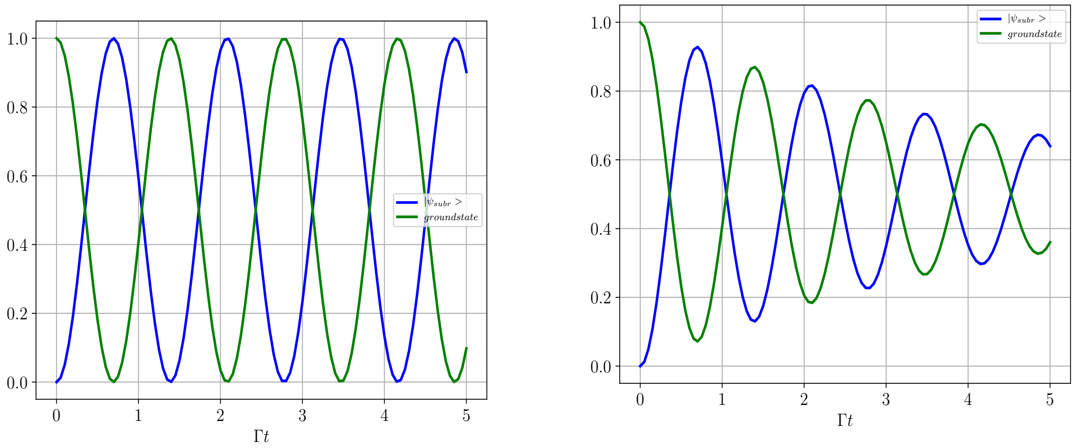

(a) Perfect Rabi oscillations.

(b) Rabi oscillations with strong damping effects on short time scale.

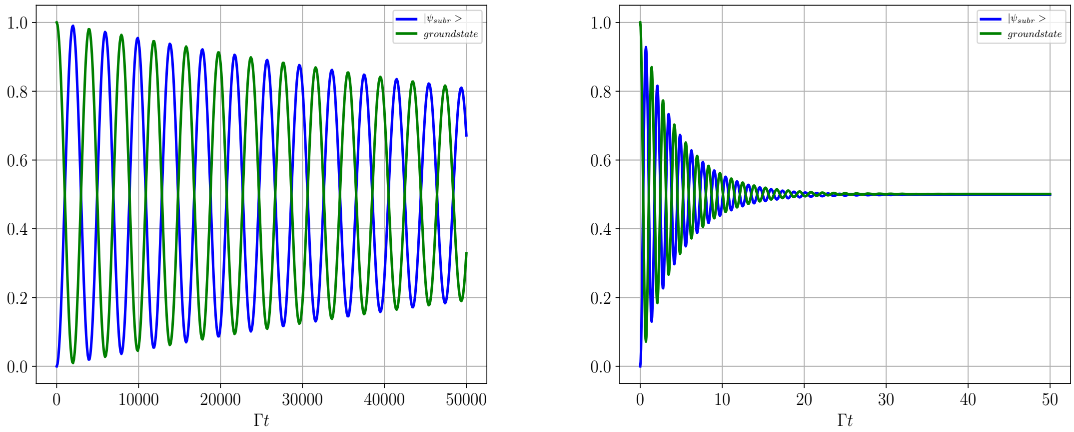

(c) Rabi oscillations, even on a very long time scale.

(d) Comparably strong lasing process for long driving.

Figure 3.10: *State preparation.* - Preparing the system in the most subradiant state of a single ring of two-level quantum emitters in the single-excitation manifold with inter-particle distance d = 0.1 (left), d = 0.4 (right) and N = 8, initially prepared in the ground state for transverse polarization. The pump strength is $\eta = 0.8\Gamma_0$.

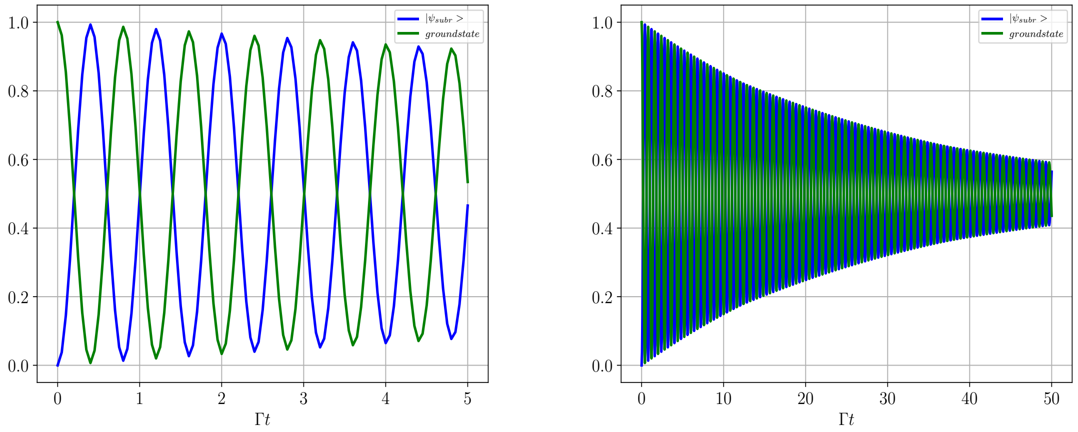

(a) Rabi oscillations.

(b) Dephasing process.

Figure 3.11: *State preparation.* - Same as in Figure 3.10, for d = 0.4, but N = 24. The system saturates slower in time by increasing the number of emitters. This goes along with the state preparation being almost perfect in that case.

any decay at all (Figure 3.13a). Contrary to that for d = 0.4 we can observe, that after applying the effective π-pulse we do not reach the subradiant state perfectly and therefore the prepared state decays very fast with a revival of the ground state (Figure 3.13b). If we increase again the number of emitters, we achieve a good matching with the wanted state and hence a comparably slow decay (Figure 3.13c).

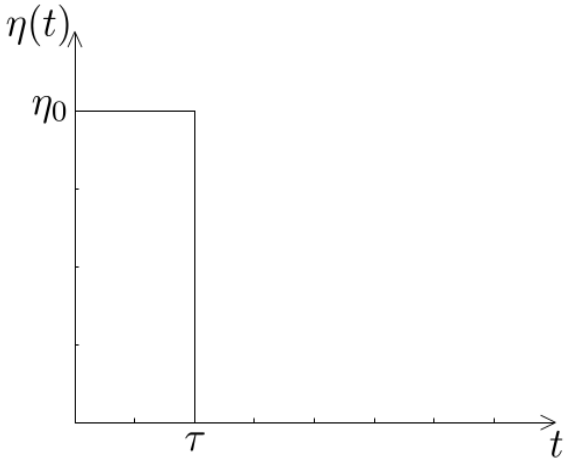

Figure 3.12: Scheme of the time dependent pump strength η(t).

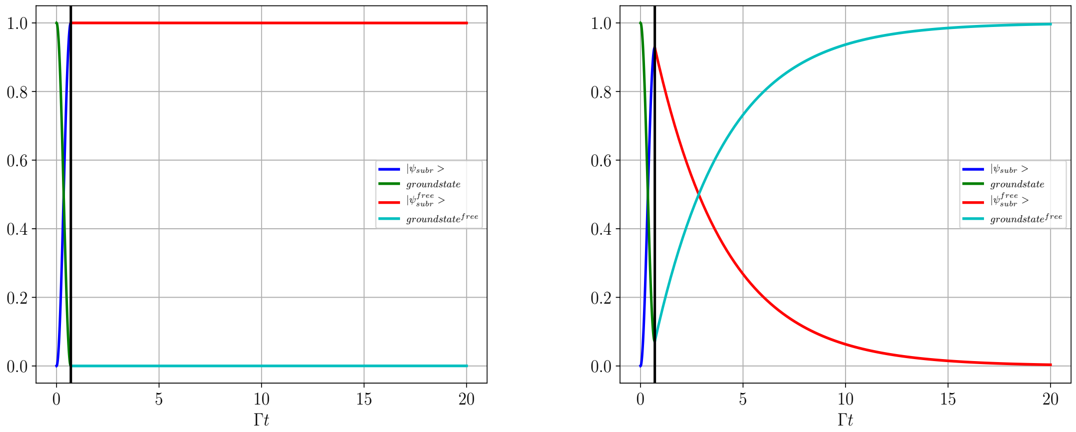

(a) d = 0.1, N = 8

(b) d = 0.4, N = 8

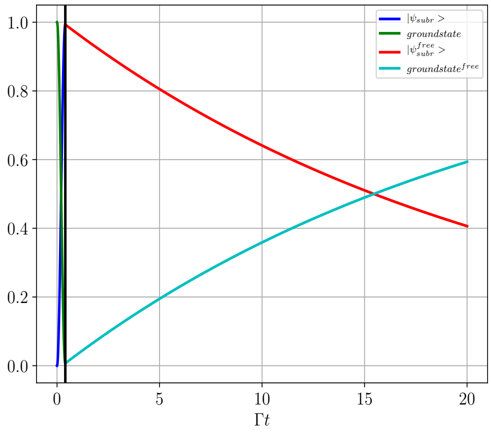

(c) d = 0.4, N = 24

Figure 3.13: *State preparation with a square pulse profile $\eta(t)$.* - Driving the most subradiant state of a single ring of two-level quantum emitters in the single-excitation manifold for different inter-particle distances d = 0.1, 0.4 and number of emitters N = 8, 24, initially prepared in the ground state. The pump strength is given in Eq. 3.9 with $\eta_0 = 0.8\Gamma_0$. The black line shows the pulse length. For d = 0.1 the system does not decay at all, whereas for d = 0.2 the decay is rather fast with a fast decay to the ground state. If we increase the number of emitters, we slow down the decay essentially.

3.2 Collective Dynamics - Two-Excitations Manifold

In this section we provide some simulations for the single ring of quantum emitters, but in the two-excitations manifold, contrary to the sections before, where we restricted ourselves to the single-excitation manifold. Additionally we will use two excitations only.

3.2.1 Some Characteristics of the Eigenvalues in the Two-excitations Manifold

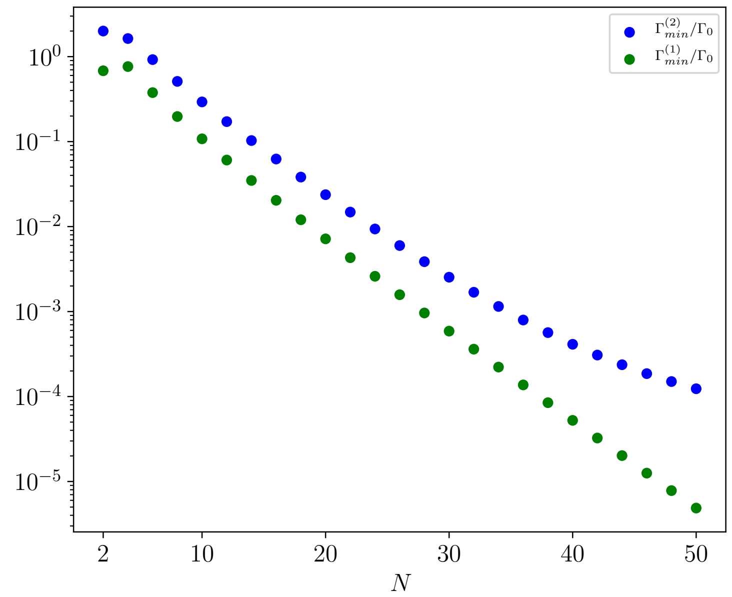

Figure 3.14: *Scaling of the most subradiant eigenmodes in the two-excitations manifold.* - Suppression in the two-excitations manifold, denoted with the index (2), compared with a single exciton state, denoted with the index (1), for R = 0.33λ and d = 0.1λ.

In Figure 3.14 we can see, that the decay of the most subradiant state with two excitations scales exponentially, such that the exponential suppression is conserved in comparison with the most subradiant exciton state in the single-excitation manifold for a growing number of quantum emitters on a ring with constant size. But there is a significant offset between these two states, so the most subradiant excitons state in the two-excitations manifold decays faster around that factor.

In Figure 3.15 the energy is defined by the polarization any longer. If the polarizations are oriented transversely, the bright modes are higher in energy, contrary to the tangential case, where the bright modes are lower in energy. But contrary to Figure 3.2, the ring in the two-excitations manifold with the smallest number of emitters experiences the biggest energy shifts for both polarizations.

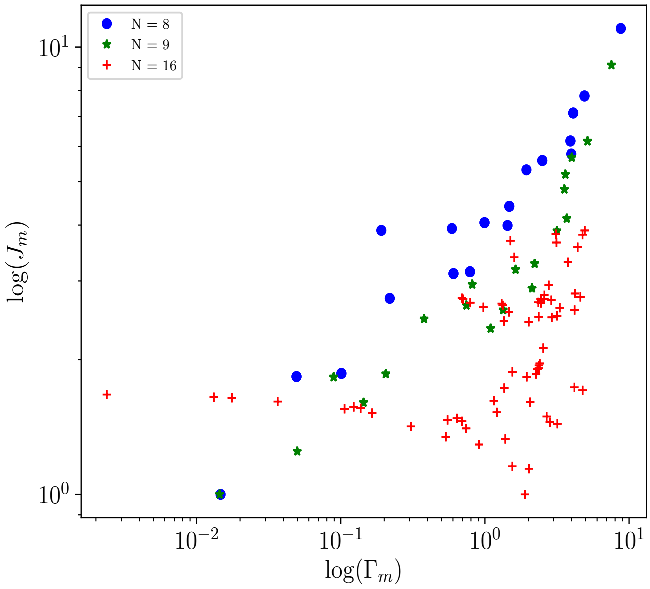

(a) Energy log-log-plot for transverse polarizations.

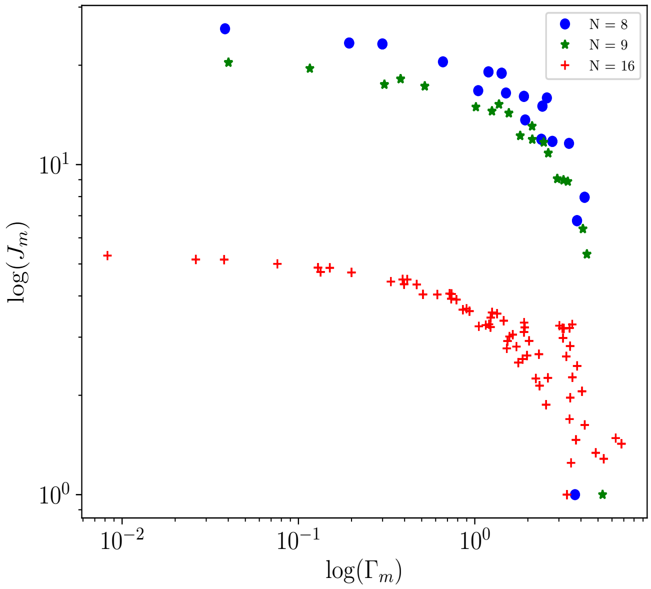

(b) Energy log-log-plot for tangential polarizations.

Figure 3.15: *Single ring energy in the two-excitations manifold with inter-particle distance $d = 0.1$ for different N for transverse and tangential polarizations, respectively.*

3.3 Radiative Properties

In this section we exhibit more of the extraordinary radiative properties of the eigenmodes of the single ring. As we could already see in the previous section 3.1, for a large enough number of emitters on the ring, we have found subradiant modes, whose emission is suppressed significantly. The suppression of the decay rates scales exponentially with the number of emitters, which is shown in Figure 3.16 for a fixed distance λ/d, in contrast to a chain of closely lying emitters scaling with N^{-3} [2]. The corresponding dark modes are characterized by a wave-vector, which is larger than the free-space wave-vector k_0, such that the eigenmodes exhibit an evanescent field transversely to the plane the ring is lying in. Therefore the light is guided nearly perfectly along the ring.

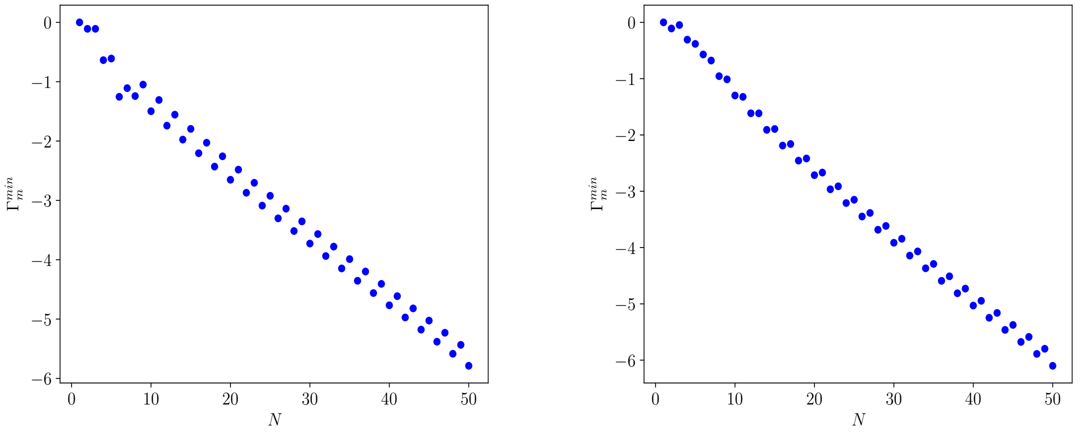

(a) Transverse polarizations.

(b) Tangential polarizations.

Figure 3.16: *Suppression.* - Logplot of Γ_m^{min} in units of Γ_0 as a function of the number of emitters. The suppression is exponential in N. For odd numbers of emitters, the decay rate is larger due to lack of symmetry.

If we now look at the electromagnetic field that is generated by subradiant modes, we can see a radiation pattern, where the field vanishes completely in the center of the ring and is evanescent transversely. For superradiant eigenmodes the field has a interference maximum at the center of the ring. Figure 3.17 shows the radiation patterns for transverse polarization in the x-y- as well as in the x-z-plane for subradiant and superradiant modes, respectively.

Figure 3.18 shows the radiation patterns for tangential polarization in the x-y- as well as in the x-z-plane for subradiant and superradiant modes, respectively.

The radiation pattern in the far field is depicted in Figure 3.19 for transverse as well as tangential polarizations, where we can see that in the case of subradiance for m = 5 the far field is also evanescent transversally and in the case of superradiance for m = 0, 1 strongly transverse, as expected.

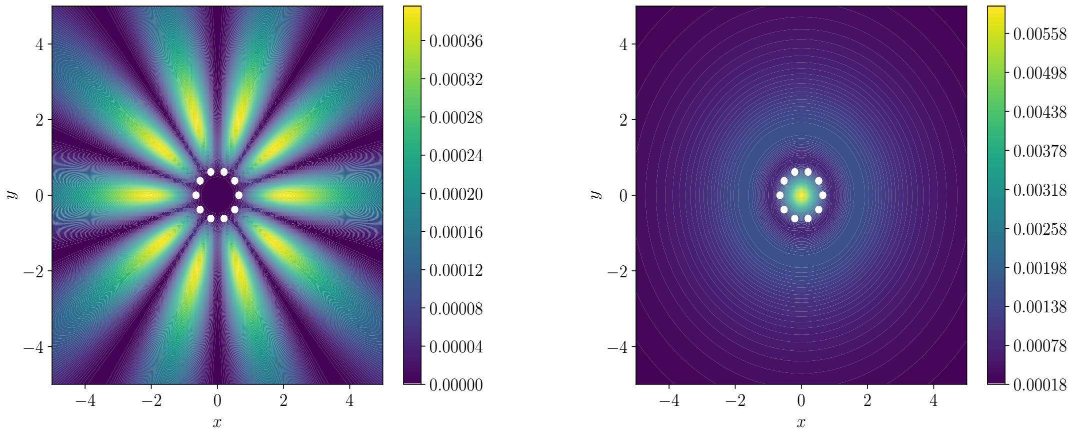

(a) Subradiant mode, xy-plane **(b)** Superradiant mode, xy-plane

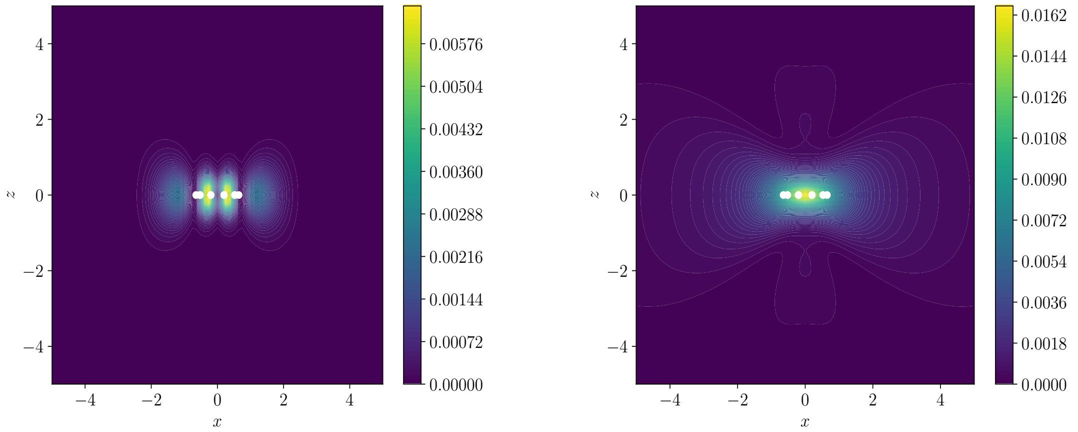

(c) Subradiant mode, xz-plane **(d)** Superadiant mode, xz-plane

Figure 3.17: *Radiation patterns of a single ring.* - Transverse polarization with distance d = 0.4λ, N = 10 and y, z = 1.5R in units of λ.

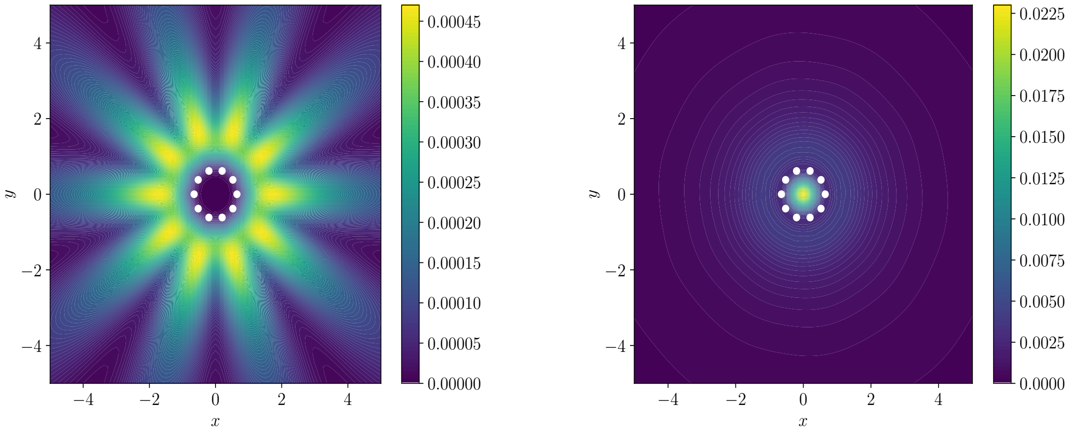

(a) Subradiant mode, xy-plane **(b)** Superradiant mode, xy-plane

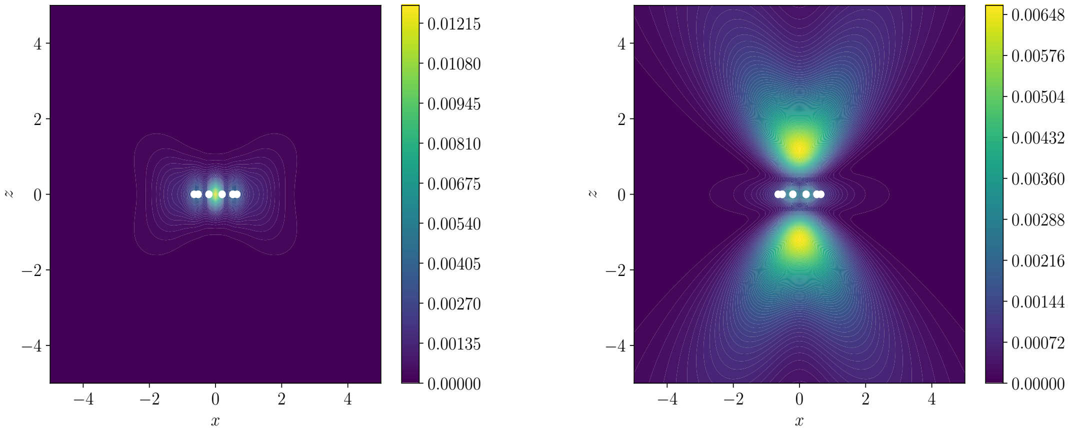

(c) Subradiant mode, xz-plane **(d)** Superadiant mode, xz-plane

Figure 3.18: *Radiation patterns of a single ring.* - Tangential polarization with distance d = 0.4λ, N = 10 and y, z = 1.5R in units of λ.

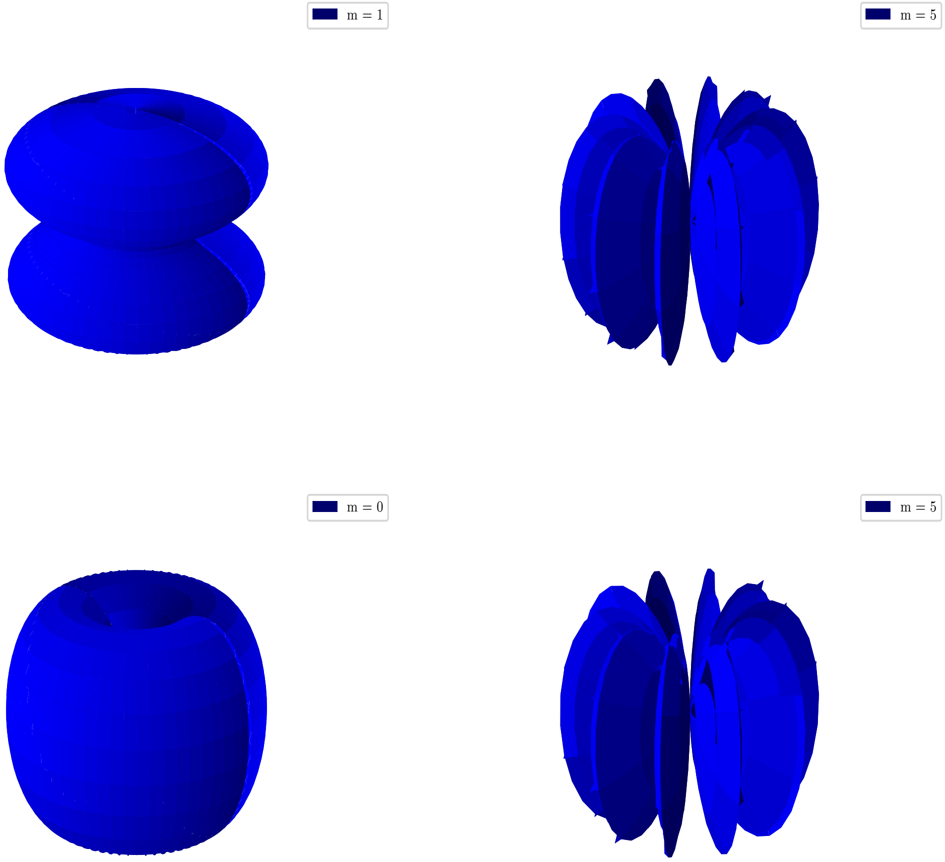

Figure 3.19: *Far field radiation patterns.* - Evaluation for r = 200R, N = 10 and d = 0.4 of a single ring lying in the x-y-plane in units of λ with transverse (left) and tangential polarizations (right).

4 Two Coupled Rings - Coupling Behavior, Excitation Transfer and Radiative Properties

In this chapter we make use of the derivations in section 2.4.2. To investigate the excitation transfer between the two rings. First we will examine the dispersive and dissipative coupling strength, respectively. With that we can evaluate the coupling efficiency to see which modes transfer the energy best. We expect that, since superradiant states carry the strongest dipole moments and couple strongly to neighboring dipoles, the dissipation in the system will be significantly higher in contrast to subradiant states. Finally, we analyze the field intensity distribution of two coupled rings.

4.1 Coupling Behavior

Equal Ring Size

In Figure 4.1 the dispersive coupling strength J_{m_1,m_2} as well as dissipative couplings Γ_{m_1,m_2} are demonstrated as functions of the angular momentum of the eigenstates in the two rings m_1 and m_2, separated by a fixed distance x = 0.15λ, for transverse and tangential polarization, respectively. In both cases, subradiant states mainly couple to subradiant states and superradiant to superradiant states. In the superradiant regime the dissipation is rather large as already mentioned before. In the case of transverse polarization, dispersive coupling uniquely occurs for superradiant states, whereby the best coupling efficiency emerges for $m_1 = \pm m_2$, but is much weaker compared to the results of tangential polarization, since the dispersive coupling appears in this case diagonally in m_1 and m_2. In each of the cases the dissipative coupling shows the least dissipation for m_1 = -m_2.

In Figure 4.1g and 4.1h we can see, that the efficiency depends strongly on the geometry of the two rings. In this case we plot the maximum value of the efficiency $\eta^{max}_{m_1,m_2}$ = $\eta_{m_1=N/2,m_2=N/2}$ as a function of the ring-to-ring separation x and can observe, that the efficiency decays exponentially oscillating down for increasing distances, whereas for transverse polarization η decays much faster than for tangential polarization. Summarized, the coupling efficiency, shown in Figure 4.1e and 4.1f, always is best for m_1 = - m_2 for small ring-to-ring distances. This indicates, that we only need a two-mode model consisting of two states m and -m, when we are working in the subradiant regime. Therefore, an excitation should oscillate between the two rings for a very long time. This very result will be used in the following section, when we study the excitation transfer of a gaussian wave-packet.

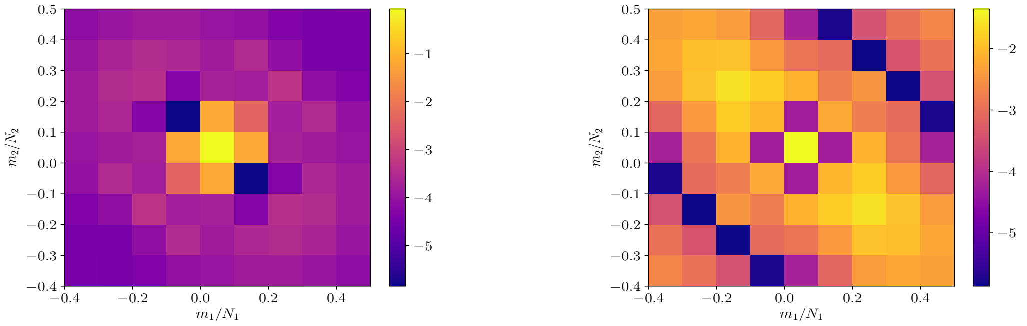

(a) J_{m_1,m_2} **(b)** J_{m_1,m_2}

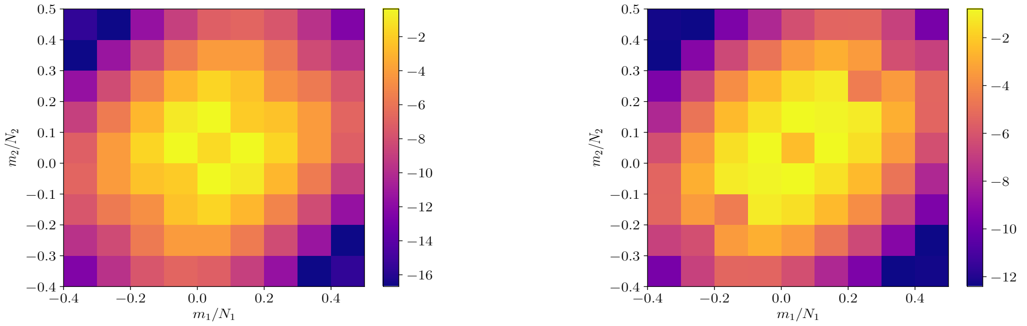

(c) Γ_{m_1,m_2} **(d)** Γ_{m_1,m_2}

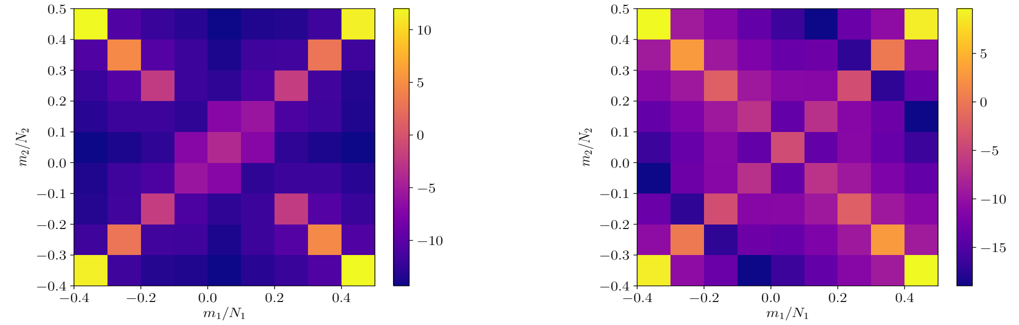

(e) η_{m_1,m_2} **(f)** η_{m_1,m_2}

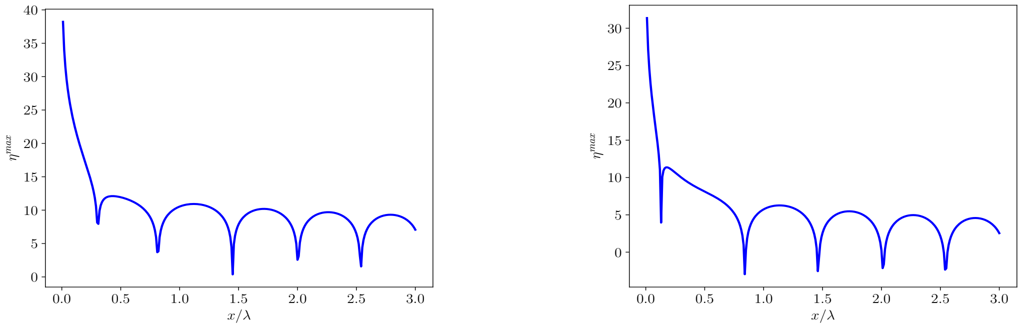

(g) Logplot of $\eta^{max}_{m_1,m_2}$ as a function of x **(h)** Logplot of $\eta^{max}_{m_1,m_2}$ as a function of x

Figure 4.1: *Two coupled rings.* - Two rings with transverse (left) and tangential (right) polarization separated by a distance x = 0.15λ with N = 10, d = 0.1λ. We show the absolute values on a logarithmic scale. The white dashed line denotes the so-called light line, where the wave-vector surpasses the free-space photon wave-vector. This is the transition line between the superradiant and the subradiant regime. Figures (g) and (f) show the logplots of the maximum valued coupling efficiency as function of the ring-to-ring distance x in units of λ.

Unequal Ring Size

In Figure 4.2 we show the same quantities as in Figure 4.1, but for different ring sizes. Here we use $N_1 = 16$ for the first ring and $N_2 = 9$ for the second one.

The dispersive couplings for the transverse polarization in the superradiant regime are rather large, but are nearly completely vanishing in the subradiant regime (Figure 4.2a). Contrary to that, the dissipation in both regimes is significant (Figure 4.2a). Therefore the coupling efficiency is only significant for $-m_1/N_1 = -m_2/N_2$, but several magnitudes lower compared to the equal sized rings. For the tangential polarization the situation is not that clear, but a closer look reveals the same behavior. The maximum value of the efficiency $\eta^{max}_{m_1,m_2} = \eta_{m_1=N/2,m_2=N/2}$ as a function of the ring-to-ring separation x shows, that the efficiency decays exponentially oscillating down for increasing distances, whereas for transverse polarization η decays much faster than for tangential polarization. But, compared to the results of the equal sized rings from before, we see again very clear the weak coupling behavior.

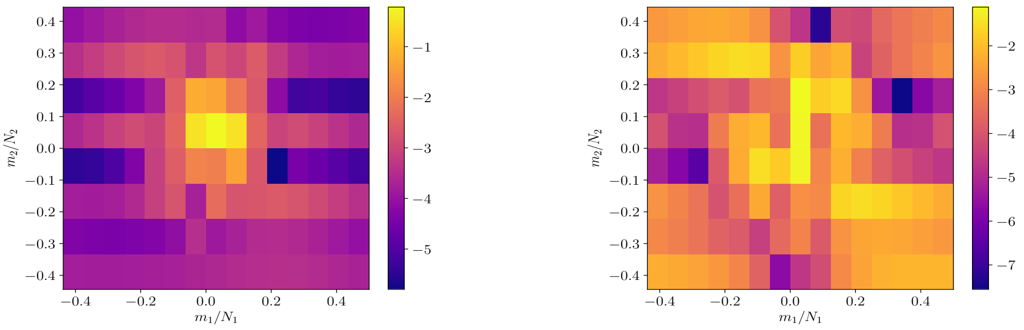

(a) J_{m_1,m_2} **(b)** J_{m_1,m_2}

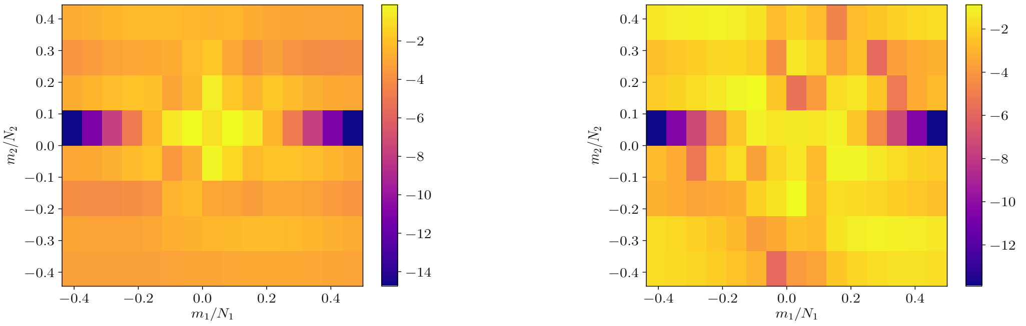

(c) Γ_{m_1,m_2} **(d)** Γ_{m_1,m_2}

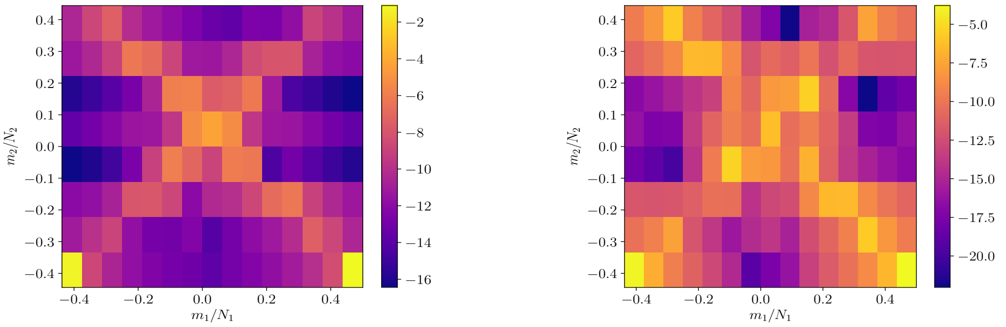

(e) η_{m_1,m_2} **(f)** η_{m_1,m_2}

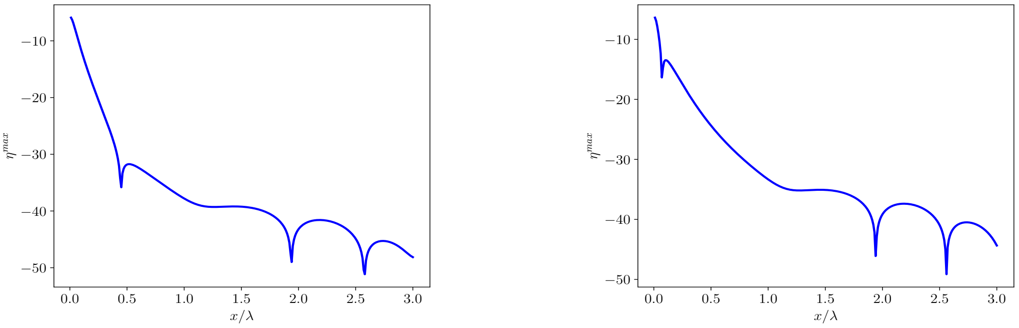

(g) Logplot of $\eta^{max}_{m_1,m_2}$ as a function of x **(h)** Logplot of $\eta^{max}_{m_1,m_2}$ as a function of x

Figure 4.2: *Two coupled rings.* - Two rings with transverse (left) and tangential (right) polarization separated by a distance x = 0.15λ with $N_1 = 16$ and $N_2 = 9$, d = 0.1λ. We evaluate the absolute values on a logarithmic scale. We reach the best coupling for $-m_1 = -m_2$, which is several magnitudes lower compared to the equal sized ring. Figures (g) and (f) show the logplots of the maximum valued coupling efficiency as function of the ring-to-ring distance x in units of λ.

4.2 Excitation Transfer

Now we evaluate the fidelity of energy transfer 2.52 for a wave-packet Eq. 2.51 centered at the site k farthest from the second ring with momentum m = N/4, depicted in Figure 4.3, where we have two rings with N = 20 separated by the distance x = 0.15λ. We observe, that the fidelity is rather low for a small wave-packet width, when the excitation is located almost perfectly at one site in real space. But even for a comparably small width in real space we can already see, that the wave-packet is localized in momentum space to exhibit good coherent excitation transport. We reach the best fidelity for a ring-to-ring distance x that approximately matches the inter-particle distance, which is intuitively understandable. Since the frequency shift of neighboring atoms is changing with their separation, they get correspondingly detuned with increasing/decreasing distance x and the excitation can not longer propagate at this point (Figure 4.3a and 4.3c). For two rings with the same size, the fidelity is extraordinarily high and shows a small damping over time (Figure 4.3b). For two rings with a different number of emitters, we observe that the fidelity is much smaller. The transport shows first a significant damping at short time and then an oscillation of the excitation between the rings for a long period without damping (Figure 4.3d). But even for a finite width, when the initial state is not a perfect eigenstate of the system, we can reach a high fidelity.

In the next step, we study the fidelity in dependence on the dipole orientation. The result is plotted in Figure 4.4, where we can see, that the fidelity for a sufficient wave-packet width θ is not limited to a narrow region of dipole polarization. Only a small area around $\pi/3$ shows a global minimum.

In Figure 4.5 we show the time evolution of the wave-packet 2.51 with a nearly infinite width θ initially centered at the site k = 10 of a ring with N = 20 atoms and angular momentum m = 5. Therefore we simulate a free evolving subradiant eigenstate of the system. The second ring is placed nearby with a distance x = 0.15. Hence, like we saw before, the excitation is hopping between the two coupled rings, while each time the sign of the angular momentum changes.

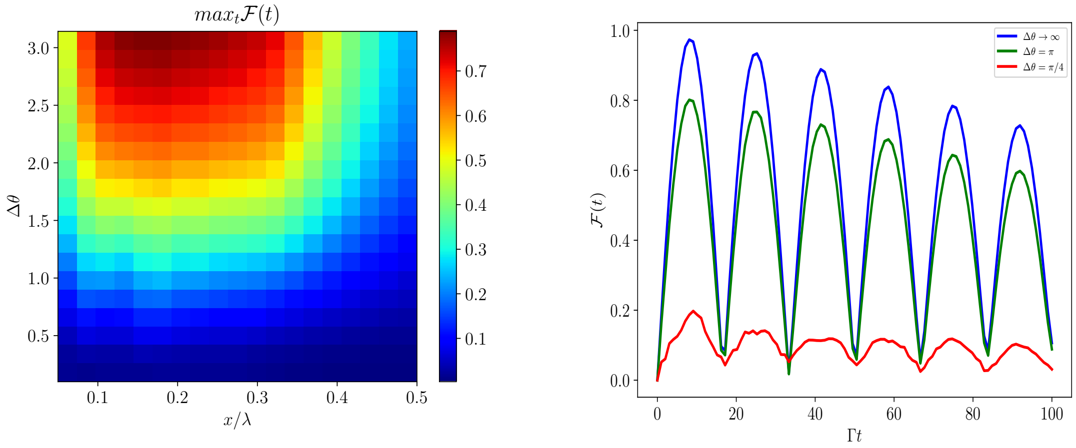

(a) Maximal fidelity over time as function of the ring separation x and the wave-packet width θ for N = 20.

(b) Fidelity $\mathcal{F}$(t) over time for two rings separated by a distance x = 0.15λ for N = 20.

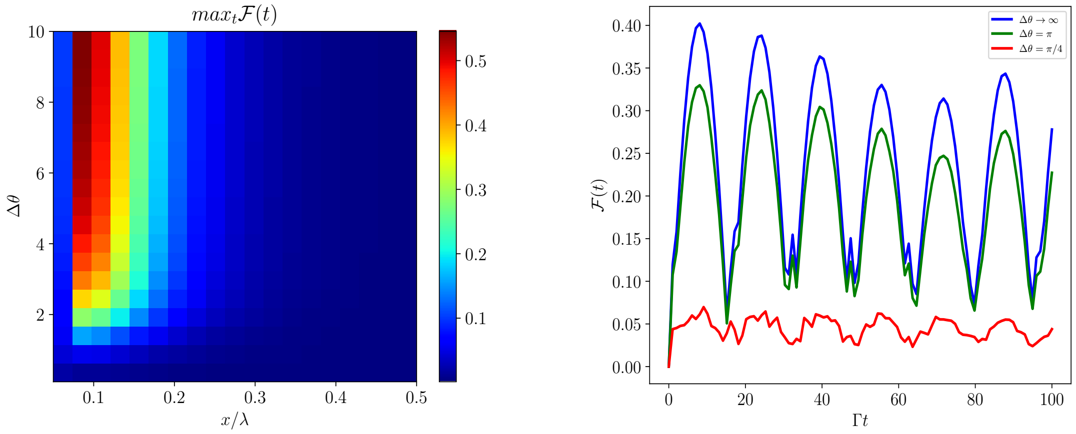

(c) Maximal fidelity over time as function of the ring separation x and the wave-packet width θ for different sized rings, $N_1 = 9$, $N_2 = 16$.

(d) Fidelity $\mathcal{F}$(t) over time for two different sized rings separated by a distance x = 0.15λ for $N_1 = 9$, $N_2 = 16$.

Figure 4.3: *Fidelity of wave-packet transport.* - Two rings with inter-particle distance d = 0.1λ and tangential polarization.

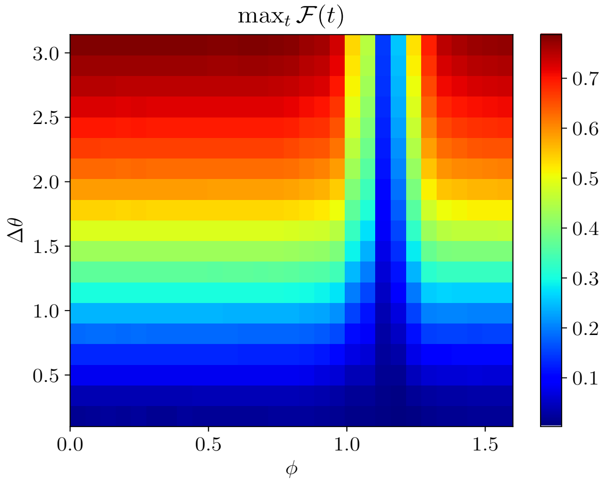

Figure 4.4: Maximal fidelity over time as a function of the dipole orientation, where $\phi = 0$ denotes tangential polarization, $\phi = \pi/2$ transverse polarization. The best fidelity can be equally achieved for both cases with a global minimum around $\pi/3$.

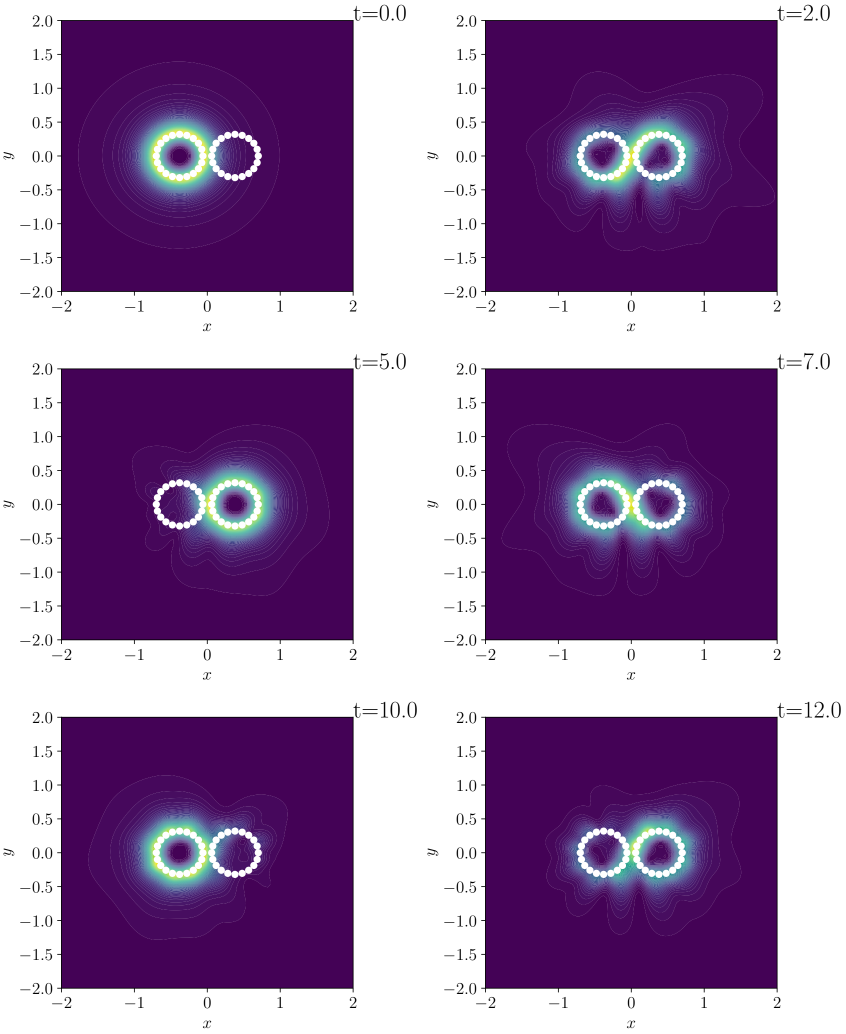

Figure 4.5: Radiation field patterns for a free evolving wave-packet initially prepared in the first ring on the left. We can see a periodic excitation transfer.

4.3 Radiative Properties

In this section we analyze the spatial field intensity distribution of coupled rings, as in Figure 4.6. Also in this case the sub- and superradiant states show distinct radiation patterns. In Figure 4.6a and 4.6b we see the field intensities for the most subradiant modes compared to the superradiant modes in Figure 6.2c and 4.6d, where the field for the subradiant cases is focussed at the region between the two rings and vanishes completely in the middle of the rings, contrary to the superradiant case, where again we have field intensity maxima at the center of the rings. This confirms, that subradiant modes mainly couple dispersively to subradiant modes, superradiant strongly couple to superradiant modes with large dissipation.

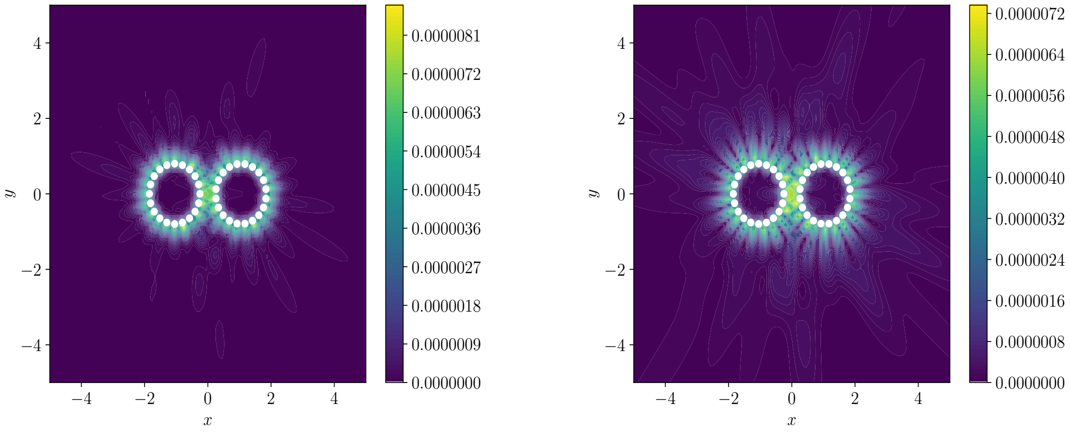

(a) Most subradiant mode **(b)** Most subradiant mode

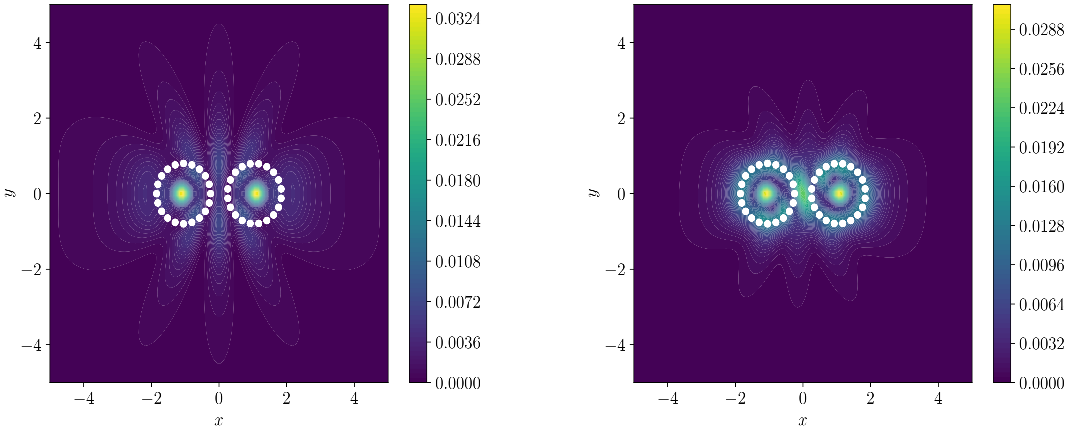

(c) Most superradiant mode **(d)** Most superradiant mode

Figure 4.6: *Field intensity of two coupled rings.* - Two rings separated by a distance x = 0.5λ with inter-particle distance d = 0.25λ, N = 20 and transverse polarization (left), tangential polarization (right).

5 Conclusion

In this master thesis we have studied the properties of an ensemble of subwavelength-spaced dipole-coupled quantum emitters, arranged in two different configurations - a single ring and two coupled rings. At the beginning we gave a brief overview of the fundamental theoretical concepts we used for developing the subsequent examinations. Then we studied the collective decay rates for the different collective excitation modes occurring in dependence of the inter-particle distance and the dipole polarization, respectively. When the emitters are close enough and transversely polarized the system shows a single bright mode with a decay rate linearly growing with the number of emitters. For tangential polarization we found two bright modes and a decay rate linearly scaling with the number of emitters divided by two. We could also show, that the dipole orientations determine, whether the bright or the dark modes are higher in energy. For a disordered, imperfect ring symmetry we saw, that regarding the subradiant state lifetime disordering seems to be beneficial for ring configurations with a primary higher inter-particle distance. We then added a driving laser to the system and presented, that by imprinting a artificial, adjusted phase on the one hand and choosing the right detuning on the other, nearly perfect Rabi oscillations between ground and dark state can be reached as well as a specific state preparation, where an effective π-pulse was implemented. Further we discussed the generated field intensities by the radiant as well as subradiant eigenmodes. In the case of subradiance the field is evanescent transversely to the plane and vanishes completely in the center of the ring , contrary to the superradiance case, where we found a strong transverse field and an interference maximum in the center of the ring. Finally, we included a further excitation to our model, since we restricted ourselves so far to the single-excitation manifold. Here we tried to find a similar approach of a effective state preparation, but were not able to identify a better phase more suitable to go beyond a state population of 1/2.

In section 3 we focused on the configuration of two coupled rings separated by a certain distance. Here we first studied the coherent and dissipative coupling strength as well as the coupling efficiency between the rings. By tailoring the geometrical parameters of this system, we found a characteristic coupling pattern, where mainly superradiant states couple to superradiant states and subradiant to subradiant states. The evaluation of the coupling efficiency indicated, that only a two-mode model is necessary. Further we analyzed the excitation transport between two coupled rings. For this we prepared a gaussian wave-packet centered at a certain site in the first ring and let it evolve freely. Using the preceding results, we were able to predict the excitation transport to the second ring. The calculated fidelity then showed a remarkable lossless coherent excitation transport, even for a state that is not a perfect eigenstate of the system.

In a nutshell, we were able to show that by tailoring the different geometrical aspects of the ring configuration and taking advantage of it, the lifetime of the excitation of an ensemble of quantum emitters can be significantly extended, whereas a very efficient state preparation can be achieved as well as a nearly lossless excitation transport between coupled rings. This work only shows the beginning of a promising approach towards an emulation of the biological role model in form of the photosynthetic LH-I-LH-II-complex for example. In future work we could plan to study more complex structures as they appear in LHC complexes, where lossless energy transport plays a vital role. Some first results are highlighted in the Appendix. Also imaginable is the exploitation of this basic model for applications in quantum computing and quantum networking.

6 Appendices

6.1 Appendix A - Program Examples

We show here a basic Julia code example written with the help of the Quantum optics toolbox QuantumOptics.jl [1] showing the calculation of the fidelity regarding the excitation transport between two coupled rings.

```julia
# Libraries
using QuantumOptics
using PyPlot
using LinearAlgebra

pygui(true)

# Parameter
λ = 1 #wavelength of an emitter
k0 = 2π #wave vector
Γ0 = 1.0 #single emitter spontaneous emission rate
d = 0.1 #inter-particle distance
ϕ = 0 #dipole orientation (here: tangential)
N = [20, 20] #number of emitters in each ring
N_tot = sum(N[i] for i=1:length(N)) #total number of emitters

# Geometry
θ(j) = [2π*(j-1)/N[1], 2π*(j-1)/N[2]];  #angle of an emitter at site j
R_ = [d/(2*sin(π/N[1])), d/(2*sin(π/N[2]))];  #radius of each ring
dips1 = [[-sin(θ(i)[1])*cos(ϕ),cos(θ(i)[1])*cos(ϕ), sin(ϕ)] for i=1:N[1]]
dips2 = [[-sin(θ(i)[2])*cos(ϕ),cos(θ(i)[2])*cos(ϕ), sin(ϕ)] for i=1:N[2]]
dips = [dips1; dips2]; #dipole orientations

# Variables
xmin = 0.05; xmax = 0.5; #ring-to-ring distance
θmin = 0.1; θmax = π; #wave-packet width
tmin = 0.; tmax = 50; #time scale
x_list = collect(range(xmin, stop=xmax, length=20))
θ_list = collect(range(θmin, stop=θmax, length=20))
t_list = collect(range(tmin, stop=tmax, length=100))

# GreenTensor
```

```
function GreenTensor(r, r_, p, k)
    R__ = r .- r_
    Rn = normalize(R__)
    n = norm(R__)
    if n == 0
        return 1.0im*k/6π .* p
    else
        Gp = exp(1.0im.*k.*n)./(4π.*n) .* ((Rn×p)×Rn .+ (1.0 ./ (k.*n).^2 .-
         ↪  1.0im./(k.*n)).*(3Rn .* (Rn·p) .- p))
        return Gp
    end
end

# Basis
basis = NLevelBasis(N_tot)
ground_state = basisstate(basis, N_tot)

# Transitions
sigma_down(i) = transition(basis, N_tot, i) #field annihilation operator
sigma_up(i) = transition(basis, i, N_tot); #field creating operator
σ_down = sigma_down.([1:N_tot;])
σ_up = sigma_up.([1:N_tot;]);


function fidelity_(x_, delta_θ)
        ψt_max = []

        r_pos1 = [[R_[1]*cos(θ(j)[1]) - R_[1] - x_/2, R_[1]*sin(θ(j)[1]), 0.0]
         ↪  for j=1:N[1]]
        r_pos2 = [[R_[2]*cos(θ(i)[2]) + R_[2] + x_/2, R_[2]*sin(θ(i)[2]), 0.0]
         ↪  for i=1:N[2]]
        r_pos = [r_pos1; r_pos2]

        # Timeevolution
        Ω(i,j) = -3*π*Γ0/k0 * real(dips[i]' * GreenTensor(r_pos[i], r_pos[j],
         ↪  dips[j], k0));
        Γ(i,j) = 6*π*Γ0/k0 * imag(dips[i]' * GreenTensor(r_pos[i], r_pos[j],
         ↪  dips[j], k0));
        H = sum((Ω(i,j) - im*Γ(i,j)/2) * sigma_up(i)*sigma_down(j) for
         ↪  i=1:N_tot, j=1:N_tot);

        m1 = 5
        m2 = 5
        k1 = 10
        ψ1(k1, delta_θ) = 1/sqrt(N[1])*sum(exp(im*m1*θ(i)[1])*exp(-norm(r_pos[i]
         ↪  .- r_pos[k1])^2/(2*R_[1]^2*delta_θ^2))*sigma_up(i)*ground_state for
         ↪  i=1:N[1]);
        ψ0 = ψ1(k1, delta_θ)
        tout, ψt = timeevolution.schroedinger(t_list, ψ0, H);
        for t=1:length(t_list)
                ψk_max = []
```

```
        # Scanning over the sites k in the second ring
        for k2=N[1]+1:2N[2]
            ψ2(k2, delta_θ) = 1/sqrt(N[2])*sum(exp(-
             ↪  im*m2*θ(j)[2])*exp(-norm(r_pos[j] .-
             ↪  r_pos[k2])^2/(2*R_[2]^2*delta_θ^2))*sigma_up(j)*ground_state
             ↪  for j=N[1]+1:2N[2]);
            ψ = norm(dagger(ψ2(k2, delta_θ))*ψt[t])
            push!(ψk_max, ψ)
        end
        push!(ψt_max, maximum(ψk_max))
    end
    return maximum(ψt_max)
end

# Plotting
fidelity_final = [fidelity_(x_, delta_θ) for x_ in x_list, delta_θ in θ_list]
z = (fidelity_final)'
pcolor(x_list, θ_list, z, cmap=ColorMap("jet"))
xlabel("x/λ")
ylabel("Δθ")
title("max t {F(t)}")
colorbar()
```

The next example gives access to the animation of excitation transport between two rings.

```
using QuantumOptics
using PyPlot
using LinearAlgebra

pygui(true)

# Parameter
λ = 1
d = 0.1
Γ0 = 1.0
k0 = 2π
x_ = 0.15 #ring-to-ring distance
ϕ = 0
N = [20, 20]
N_tot = sum(N[i] for i=1:length(N))
Ncum = cumsum(N)

# Geometry
θ(j) = [2π*(j-1)/N[1], 2π*(j-1/2)/N[2]]
R_ = [d/(2*sin(π/N[1])), d/(2*sin(π/N[2]))]

r_pos1 = [[R_[1]*cos(θ(j)[1]) - R_[1] - x_/2, R_[1]*sin(θ(j)[1]), 0.0] for
 ↪  j=1:N[1]]
```

```
r_pos2 = [[R_[2]*cos(θ(i)[2]) + R_[2] + x_/2, R_[2]*sin(θ(i)[2]), 0.0] for i=1:N[2]]
r_pos = [r_pos1; r_pos2]

dips1 = [[-sin(θ(i)[1])*cos(ϕ),cos(θ(i)[1])*cos(ϕ), sin(ϕ)] for i=1:N[1]]
dips2 = [[-sin(θ(i)[2])*cos(ϕ),cos(θ(i)[2])*cos(ϕ), sin(ϕ)] for i=1:N[2]]
dips = [dips1; dips2]

#GreenTensor
function GreenTensor(r, r_, p, k)
    R__ = r .- r_
    Rn = normalize(R__)
    n = norm(R__)
    if n == 0
        return 1.0im*k/6π .*p
    else
        Gp = exp(1.0im.*k.*n)./(4π.*n) .* ((Rn×p)×Rn .+ (1.0 ./ (k.*n).^2 .- 1.0im./(k.*n)).*(3Rn .* (Rn⋅p) .- p))
        return Gp
    end
end

# Basis
basis = NLevelBasis(N_tot+1)
ground_state = basisstate(basis, N_tot+1)

# Transitions
sigma_down(i) = transition(basis, N_tot+1, i)
sigma_up(i) = transition(basis, i, N_tot+1);
σ_down = sigma_down.([1:N_tot;])
σ_up = sigma_up.([1:N_tot;]);


# Collective coupling, Decay rate
Ω(i,j) = -3*π*Γ0/k0 * real(dips[i]' * GreenTensor(r_pos[i], r_pos[j], dips[j], k0))
Γ(i,j) = 6*π*Γ0/k0 * imag(dips[i]' * GreenTensor(r_pos[i], r_pos[j], dips[j], k0))

#######Hamiltonians
H_dipole = sum(Ω(i,j)*sigma_up(i)*sigma_down(j) for i=1:N_tot, j=1:N_tot)
eigenvalues_dip, eigenvectors_dip = eigenstates(dense(H_dipole))

#Decay rates, position subradiant, superradiant state
decay_rates = [real(expect(projector(eigenvectors_dip[k]), sum(Γ(i,j)*sigma_up(i)*sigma_down(j) for i=1:N_tot, j=1:N_tot))) for k=1:length(eigenvalues_dip)]


# Initial state
delta_θ = 100 #wave-packet width
```

```
m1 = 5 #angular momentum
k1 = 10 #site index
ψ1 = 1/sqrt(N[1])*sum(exp(im*m1*θ(i)[1])*exp(-norm(r_pos[i] .- r_pos[k1])^2/(2*R_[1]^2*delta_θ^2))*sigma_up(i)*ground_state for i=1:N[1]);

# Time scale
tmin = 0.; tmax = 30
t_list = collect(range(tmin, stop=tmax, length=80))


# Field
function e_field(r)
    field = [0*σ_down[1] for i=1:3]
    for i=1:N_tot
        G_ = GreenTensor(r, r_pos[i], dips[i], k0)
            for j=1:3
                field[j].data .+=  G_[j] .* σ_down[i].data
            end
    end
    return field
end


#Intensity of the field
function Intensity(r)
    E = e_field(r)
    sum(dagger(e)*e for e=E)
end

# Timeevolution
H = sum((Ω(i,j) - im*Γ(i,j)/2) * sigma_up(i)*sigma_down(j) for i=1:N_tot, j=1:N_tot);
tout, ψt = timeevolution.schroedinger(t_list, ψ1, H)


# Points in space
xmin = -3; xmax = 3;
x = collect(range(xmin, stop=xmax, length=100))
y = collect(range(xmin, stop=xmax, length=100))
z = 2*d
r_space = [[r1, r2, r3] for r1=x, r2=y, r3=z]

# Expectation value, Intensity
Intensity_exp(r, ψ) = real(expect(Intensity(r), ψ));

Intensity_final = [[Intensity_exp(r_, ψt[t]) for r_=r_space] for t=1:length(t_list)]


# Plotting
figure(figsize=(15,12))
```

```
for i=1:N_tot
    plot(r_pos[i][1], r_pos[i][2], "wo")
end

fig1=figure(figsize=(15,12))
subplot(321)
contourf(x, y, (Intensity_final[1])', 100)
annotate(xy=[2, 2], s="t=(round(t_list[1];))", fontsize=20)
subplot(322)
contourf(x, y, (Intensity_final[10])', 100)
annotate(xy=[2, 2], s="t=(round(t_list[10];))", fontsize=20)
subplot(323)
contourf(x, y, (Intensity_final[20])', 100)
annotate(xy=[2, 2], s="t=(round(t_list[20];))", fontsize=20)
subplot(324)
contourf(x, y, (Intensity_final[30])', 100)
annotate(xy=[2, 2], s="t=(round(t_list[30];))", fontsize=20)
subplot(325)
contourf(x, y, (Intensity_final[40])', 100)
annotate(xy=[2, 2], s="t=(round(t_list[40];))", fontsize=20)
subplot(326)
contourf(x, y, (Intensity_final[50])', 100)
annotate(xy=[2, 2], s="t=(round(t_list[50];))", fontsize=20)
tight_layout()

using Printf
using PyCall
anim=pyimport("matplotlib.animation")
pygui(true)

fig=figure(1)
function animate(t)
  t+=1
  contourf(x, y, (Intensity_final[t])', 100)
  annotate(xy=[2, 2], s="t=(round(t_list[t];))", fontsize=20)
  title("t="*@sprintf("\%03.2f",t_list[t]))
  xlabel(L"x")
  ylabel(L"y")
end
movie=anim.FuncAnimation(fig, animate, frames=length(t_list),repeat=false, interval=20)
```

6.2 Appendix B - Multi-ring: A simplistic Recreation of LHCs

Here we provide field intensity simulations in the single-excitation manifold for a multi-ring configuration inspired photosynthetic units of diverse biological systems. Those light harvesting complexes are present in certain types of bacteria, for example Rs. molischianum or Rps. acidophila. The photosynthetic apparatus of purple bacteria is constructed by two different kinds of pigment-protein complexes, on the one hand the reaction centre, on the other hand the light harvesting complexes [18]. The light harvesting complexes capture light energy and transfer this energy to the reaction centre for photo-induced redox processes. The photosynthetic membranes of the most purple bacteria consist of two types of light harvesting complexes, the light harvesting complex I (LH-I) and the light harvesting complex II (LH-II). The LH-I is tightly bound to the photosynthetic reaction centre built by independent pigments in the center of the LH-I, whereas the LH-II, not directly connected to the reaction centre, is needed to transfer the energy to the reaction centre via the LH-I, like depicted in Figure 6.1c [18]. The LH complexes are composed by ring-shaped proteins, whereas the optical active parts consist mostly of BChl molecules and Carotenoids. The molecules crystallize regularly in a ring configuration. This is exemplary shown in Figure 6.1a, where each of the n molecules corresponds to a different site forming a ring.

If the antenna complex now harvests sunlight and makes the energy available to the reaction centre through the series of energy transfer steps between the complexes mentioned above, then the dynamics occurring here take place in the piko seconds regime and are very efficient. The excitation transfer is strongly hierarchic, which is shown in Figure 6.1b, where the excitation is cascading into the reaction centre. The processes can be distinguished between inter- and intra-complex processes, described as excitation transfer *within* each pigment-protein complex, therefore LH-II, LH-I and RC, and *between* pigment-protein complexes, hence LH-II $\rightarrow$ LH-II, LH-II $\rightarrow$ LH-I and LH-I $\rightarrow$ RC, respectively [18]. A schematic drawing is depicted in Figure 6.1c, where a typical bacterial photosynthetic unit is shown. The LH-II contains two types of BChl, B850 and B800, the LH-I contains just on type of BChl, B875. The light gets harvested on the most outer ring and the excitation then gets transported into the reaction centre. The excitation transfer here in the photosynthetic unit between LH-II,LH-I and finally the reaction centre occurs in less than 100 pico seconds and reaches an efficiency of around 95% [23]. The transition dipole moments of the B850 and B875 BChls are all oriented in the two-dimensional plane spanned by the BChl molecules, such that the electronic excitation flow is optimally tuned [18]. Besides other potential pathways for photons, one example could be the absorption of an 800nm photon by one of the B800 BChls in LH-II. This excitation then gets transferred via the B850 BChl and the B875 BChl in the LH-I to the reaction centre, where femtosecond spectroscopy reveals that the B800 $\rightarrow$ B850 process needs 700fs and the B850 $\rightarrow$ B875 process just $3 \approx 5$ ps. The final step of LH-I $\rightarrow$ RC needs more or less 35 ps, which is the slowest process [18]. The energy transfer between both BChls B800 and B850 can be explained by the Förster mechanism, where an exciton splitting takes place, which greatly improves the resonance of the excitations of B800 and B850 [18] [24] [25]. The carotenoids absorb light at 500nm and play a role of light harvesting, roughly spoken. By quenching the BChl triplet states, they also protect the light-harvesting system from the damaging effect of BChl triplet states, which can generate highly reactive singlet oxygen [18]. The overall ring structure can be explained by the fact, that the resonance between donor and

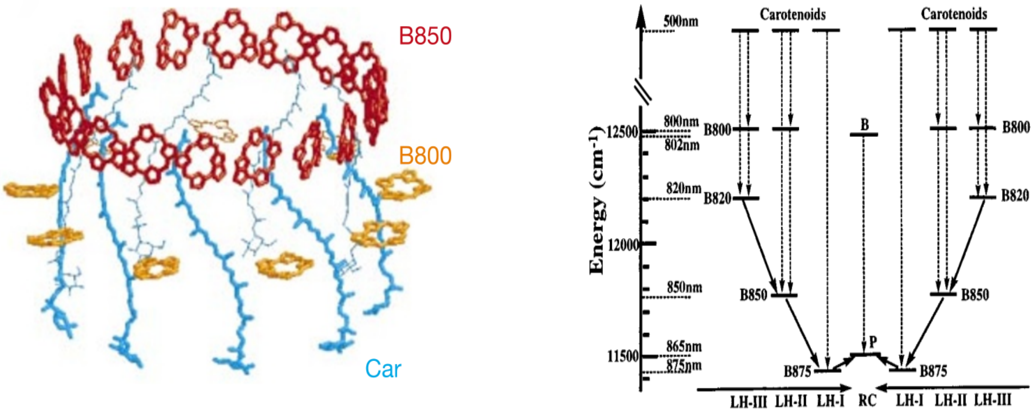

(a) Geometrical arrangement in LH-II complexes of R. acidophila of the carotenoid ('Car') in blue and bchl molecules in orange (B800) and red (B850), whereas the numbers stand for the absorption wavelength in nm [19].)

(b) Energy levels of the electronic excitations in the photosynthetic unit in purple bacteria. The funneling of excitation toward the photosynthetic reaction centre is shown.

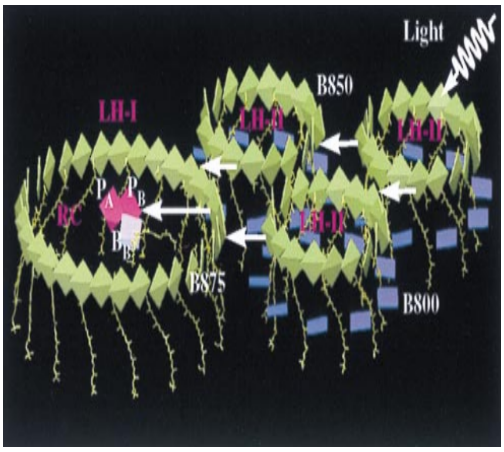

(c) Schematic figure of the excitation transfer in a bacterial photosynthetic unit.

Figure 6.1: *Properties of a photosynthetic unit in purple bacteria.*

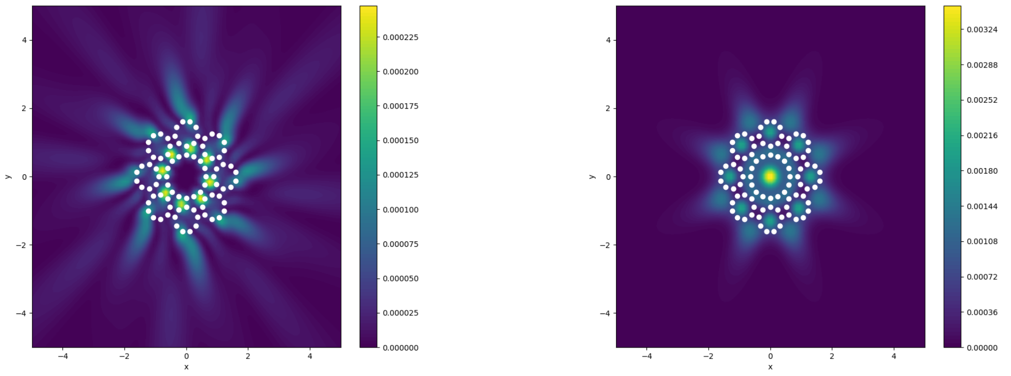

(a) Outer rings: most subradiant mode - Inner ring: most subradiant mode

(b) Outer rings: most superradiant mode - Inner ring: most subradiant mode

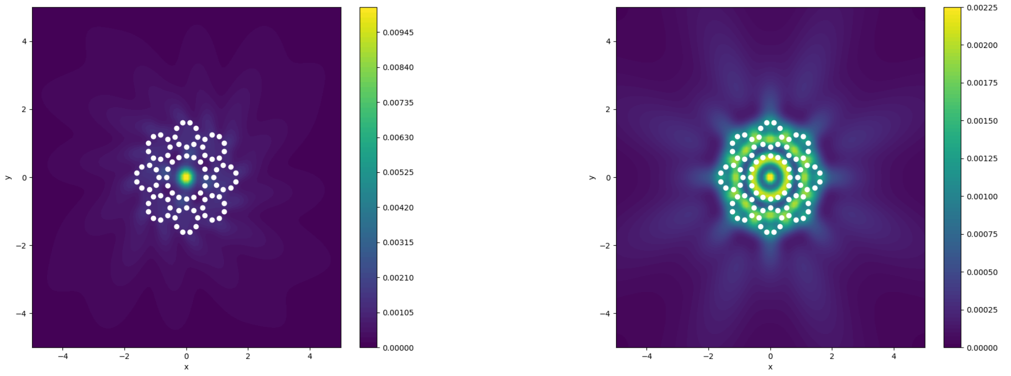

(c) Outer rings: most subradiant mode - Inner ring: most superradiant mode

(d) Outer rings: most superradiant mode - Inner ring: most superradiant mode

Figure 6.2: *Field intensity of a multi ring configuration with transverse polarization.* - One inner ring with $N_{in} = 16$ surrounded by eigth outer rings with each $N_{ou} = 9$ emitters. The rings are separated by a distance x, y = 0.25λ with inter-particle distance d = 0.25λ.

acceptor systems can be improved by that and therefore the exciton splitting leads to a faster, more efficient transfer time [18].

In Figure 6.2 and 6.3 we show the field intensity in the single-excitation manifold for a multi-ring configuration, where eight outer rings with each nine emitters are coupled to a larger inner ring with 16 emitters. The outer rings can be understood as LH-II complexes that are coupled to LH-I, in which center the reaction centre lies. We study this configuration for transverse as well as tangential polarization and assume, that the outer rings are uniformly in one state and the inner ring is in one specific state. We can observe that the excitation is located perfectly in the middle of the multi-ring with a evanescent field tangentially in the case of a collective subradiant state for the outer rings and superradiant state for the inner ring.

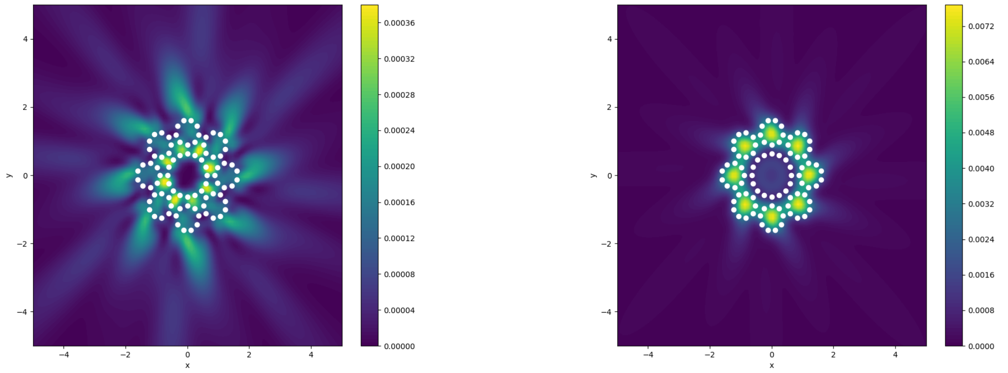

(a) Outer rings: most subradiant mode - Inner ring: most subradiant mode

(b) Outer rings: most superradiant mode - Inner ring: most subradiant mode

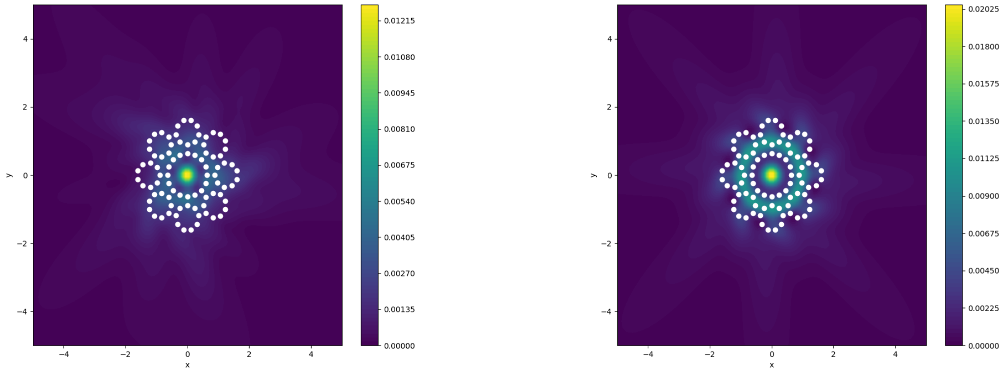

(c) Outer rings: most subradiant mode - Inner ring: most superradiant mode

(d) Outer rings: most superradiant mode - Inner ring: most superradiant mode

Figure 6.3: *Field intensity of a multi ring configuration with tangential polarization.* - One inner ring with $N_{in} = 16$ surrounded by eigth outer rings with each $N_{ou} = 9$ emitters. The rings are separated by a distance x, y $= 0.25\lambda$ with inter-particle distance d $= 0.25\lambda$.

Bibliography

[1] S. Kraemer, D. Plankensteiner, L. Ostermann, and H. Ritsch *Comput. Phys. Commun. 227, 109*, 2018.

[2] A. Asenjo-Garcia, M. Moreno-Cardoner, A. Albrecht, H. J. Kimble, and D. E. Change *Phys. Rev. X 7, 031024*, 2017.

[3] R. H. Dicke *Phys. Rev. 93, 99*, 1954.

[4] K. Hammerer, A. S. Sorensen, and E. S. Polzik *Rev. Mod. Phys. 82, 1041*, 2010.

[5] P. Solano, P. Barberis Blostein, F. K. Fatemi, L. A. Orozco, and S. L. Rolston *arXiv: 1704.07486*, 2017.

[6] W. Guerin, M. O. Araujo, and R. Kaiser *Phys. Rev. Lett. 116, 083601*, 2016.

[7] R. G. DeVoe and R. G. Brewer *Phys. Rev. Lett. 76, 2049*, 1996.

[8] L. V. Hau, S. E. Harris, Z. Dutton, and C. H. Behroozi *Nature (London) 397, 594*, 1999.

[9] M. Fleischhauer, A. Imamoglu, and J. P. Marangos *Rev. Mod. Phys. 77, 633*, 2005.

[10] B. Julsgaard, A. Kozhekin, and E. S. Polzik *Nature (London) 413, 400*, 2001.

[11] J. Pritchard, K. Weatherill, and C. Adams *World Scientific, Singapore, pp. 301 until 350*, 2013.

[12] W. Wasilewski, K. Jensen, H. Krauter, J. J. Renema, M. V. Balabas, and E. S. Polzik *Phys. Rev. Lett. 104, 133601*, 2010.

[13] M. Moreno-Cardoner, D. Plankensteiner, L. Ostermann, D. Chang, and H. Ritsch *arXiv:1901.10598*, 2019.

[14] P. O. Guimond, A. Grankin, D. Vasilyev, B. Vermersch, and P. Zoller *arXiv:1901.02665*, 2019.

[15] M. L. Brongersma, J. W. Hartman, and H. A. Atwater *Physical Review B 62, R16356*, 2000.

[16] A. Serafini, S. Mancini, and S. Bose *Physical review letters 96, 010503*, 2006.

[17] R. J. Cogdell, A. Gall, and J. Koehler *Q. Rev. Biophys. 39, 227*, 2006.

[18] X. Hu, et al. *J. Phys. Chem. B 101, 3854-3871*, 1997.

[19] J. L. Herek et al. *Nature 417, 533*, 2002.

[20] D. Plankensteiner, *Collective Dynamics and Spectroscopy of Coupled Quantum Emitters.* PhD thesis, Leopold-Franzens-Universitaet Innsbruck, 2019.

[21] L. Ostermann, *Collective Radiation of Coupled Atomic Dipoles and the Precise Measurement of Time.* PhD thesis, Leopold-Franzens Universitaet Innsbruck, 2016.

[22] D. Plankensteiner, "Exploiting collective effects in a system of interacting quantum emitters," Master's thesis, Leopold-Franzens Universitaet Innsbruck, 2014.

[23] T. Pullerits, V. Sundstrom *Acc. Chem. Res 29, 381-389*, 1996.

[24] T. Foerster *Ann. Phys. 2, 55-75*, 1948.

[25] J.R. Oppenheimer *Phys. Rev. 60, 158*, 1941.